SUPPLEMENTARY MATERIAL 1

Molecular determinants of pro-arrhythmia proclivity of d- and l-sotalol via a multi-scale modeling pipeline

Kevin R. DeMarco[1], Pei-Chi Yang[1], Vikrant Singh[2], Kazuharu Furutani[1,3], John R. D. Dawson[1,4], Mao-Tsuen Jeng[1], James C. Fettinger[5], Slava Bekker[1,6], Van A. Ngo[7], Sergei Y. Noskov[7], Vladimir Yarov-Yarovoy[1,8], Jon T. Sack[1,8], Heike Wulff[2], Colleen E. Clancy, [1,2] and Igor Vorobyov[1,2*]

[1] Department of Physiology and Membrane Biology, University of California Davis, Davis, CA 95616, USA

[2] Department of Pharmacology, University of California Davis, Davis, CA 95616, USA

[3] Department of Pharmacology, Faculty of Pharmaceutical Sciences, Tokushima Bunri University, Tokushima, Tokushima 770-8514, Japan

[4] Biophysics Graduate Group, University of California Davis, Davis, CA 95616, USA

[5] Department of Chemistry, University of California Davis, Davis, CA 95616, USA

[6] Department of Science and Engineering, American River College, Sacramento, CA 95841, USA

[7] Centre for Molecular Simulation and Biochemistry Research Cluster, Department of Biological Sciences, University of Calgary, Calgary, AB T2N1N4, Canada

[8]Department of Anesthesiology and Pain Medicine, University of California Davis, Davis, CA 95616, USA

[*] Correspondence to:
Igor Vorobyov
University of California, Davis
Department of Physiology and Membrane Biology
4303 Tupper Hall,
One Shields Ave,
Davis, CA 95616-8636, USA

E-mail: ivorobyov@ucdavis.edu

S1. Supplementary Methods

S1.1. Atomistic Simulations

***Ion channel model**:* Our previously published atomistic structural open-state hERG channel model [1], based on the cryo-EM structure with 3.80 Å resolution [2] (PDB ID: 5VA2) comprises residues 405-668 of homotetrameric voltage sensing domain (VSD) and pore domain (PD) with intracellular domains truncated. Symmetry-imposed local iterative refinement and fragment-based loop modeling protocols [3-5] in Rosetta structural modeling software were used to generate loop regions not resolved from cryo-EM density data.

***Drug force field**:* Previously published all-atom force field parameters for cationic and neutral sotalol [6] were based on initial guesses from general CHARMM (Chemistry at Harvard Molecular Mechanics) force field (CGENFF) program [7, 8]. Initial guesses for parameters with poor chemical analogy were optimized with the ffTK plugin [9] for the Visual Molecular Dynamics program (VMD) [10]. Gas-phase QM calculations utilizing Møller–Plesset second-order perturbation theory (MP2) and Hartree-Fock approximation (HF) with the 6-31(d) basis set in Gaussian 09 program [11] were used to compute target data for parameter optimization [12].

***General MD simulation setup**:* The CHARMM-GUI online toolkit [13], NAMD [14], and Anton 2 software [15] programs were used in order to build and simulate the molecular systems in this study. All of them contained our open-state hERG channel model [1] embedded in a 1-palmitoyl-2-oleoylphosphatidylcholine (POPC) lipid bilayer hydrated by a 0.15 M aqueous KCl solution. The membrane normal axis was aligned along the *z*-axis in simulated systems. The hERG channel was placed in the bilayer center with its aqueous pore aligned with the membrane normal. CHARMM36 all-atom force fields for protein and lipids [16-18] as well as TIP3P water model [19] were used in all MD simulations in this study. Assembled systems consisted of about 132,000 – 133,000 atoms and were simulated with NAMD 2.13 [14] in the *NPT* ensemble with 1 atm pressure maintained by Langevin piston barostat [20], and 310K,

controlled by Nosé-Hoover thermostat [21, 22]. Tetragonal cells with periodic boundary conditions (PBC) were used in all the simulations, and the SHAKE algorithm [23] was employed to fix the bonds to all hydrogen atoms, allowing for the use of a 2 fs time step. Electrostatic interactions were computed via Particle Mesh Ewald [24], with a mesh grid of 1 Å.

Drug – protein flooding simulations: The special-purpose Anton 2 supercomputer [15] from DE Shaw research allowed for multi-microsecond unbiased drug flooding MD simulations, in which drug molecules were initially placed in bulk aqueous solution and allowed to freely sample the system. These simulations were used to elucidate possible d- and l-sotalol hERG entry and egress pathways. They were initiated from building molecular systems containing our open hERG channel model [1] embedded in a POPC lipid bilayer solvated in 0.15 M KCl aqueous solutions, also containing 23 molecules or ~0.05 M initial aqueous concentration of cationic (+) or neutral (0) d- or l-sotalol (4 systems total). Drug molecules were randomly placed in the hERG channel simulation system box excluding lipid membrane position and the protein itself and also ensuring optimal distances between adjacent molecules. A hydrated lipid bilayer was added using CHARMM-GUI [25], and the entire system was equilibrated for 90 ns with NAMD 2.13 in the *NPT* ensemble at 310 K and 1 atm pressure using the same protocol as in our previous study [1, 26], and the system sizes and compositions were similar to those described above. A custom restraint regime was implemented over a prolonged equilibration period of 40 ns in order to ensure overall stability of the model and sufficient pore hydration [1, 26], and then each system was run for 50 ns unrestrained. The equilibrated systems were further simulated on Anton 2 using software version 1.27.0 in the *NPT* ensemble for 8 μs for each of d-sotalol(+), d-sotalol(0), l-sotalol(+) and l-sotalol(0) systems. Multigrator algorithm [27] was used for temperature and pressure control with semi-isotropic 1 atm pressure coupling using Martyna, Tobias, and Klein (MTK) barostat [28] and temperature coupling at 310 K with Nosé-Hoover thermostat [21, 22]. Optimal non-bonded cutoffs for each system were determined using default Anton 2 software settings, and the *u*-series, Gaussian-based decomposition method, [15] was used for long-range electrostatic interactions.

***Umbrella sampling MD (US-MD) and Hamiltonian replica exchange US-MD (HREUS-MD) simulations*:** US-MD simulations [29] were used to sample drug interaction with the hERG channel pore, and free energy or potential of mean force (PMF), ΔG, profiles were computed using weighted histogram analysis method (WHAM) [30]. These simulations began with an initial equilibration run, in which the drug was harmonically restrained in bulk aqueous solution at z=–50 Å with respect to the selectivity filter (SF) C_α center of mass (COM) and allowed to rotate freely. After 50 ns of equilibration, 5 different initial configurations were chosen to begin steered molecular dynamics (SMD) [31] runs, in which the drug was pulled, in 0.5 Å increments for each 1 ns of the simulations, at constant applied force, from bulk water (z=–50 Å) to a point in the pore 5.5 Å below the SF COM of selectivity filter (z=–5.5 Å). From these SMD trajectories, initial US-MD windows were chosen at random for corresponding drug z positions as we outlined previously [1, 26]. There were 90 independent US-MD windows with 10.0 kcal/mol/Å^2 harmonic restraint, spaced in 0.5 Å intervals for -50 Å $\leq z \leq -5.5$ Å with respect to the COM of hERG SF C_α atoms. The pore domain (PD) C_α and all SF backbone non-H atoms were subject to 1.0 kcal/mol/Å^2 harmonic restraints during initial equilibration and steered MD runs. Those restraints were gradually reduced to 0.2 kcal/mol/Å^2 during first 5 ns of each US-MD run and then maintained throughout US-MD and HREUS-MD simulations to prevent channel transition to a different conformational state. An additional cylindrical flat-bottom harmonic restraint with a width of 10 Å and a force constant 5 kcal/mol/Å^2 was applied in order to prevent drift of the drug in the xy plane using the collective variables (COLVAR) functionality of NAMD as outlined previously [1, 26]. All US-MD were run using NAMD for 50 ns per US-MD window (4,500 ns in total) with first 10 ns discarded. HREUS-MD simulations [32] were performed to sample drug reorientation in the channel pore, which was hindered to transition during conventional US-MD runs. Those simulations started at the end of 20 ns of each US-MD run and ran for 60 ns per window (5,400 ns in total). During those runs adjacent window umbrella potentials were exchanged randomly every 1,000 MD steps (2 ps), and such exchanges were accepted or rejected using Metropolis criterion. At the end of HREUS-MD simulations the replicas were sorted to obtain drug z position distributions as in US-MD runs

and subjected to WHAM analysis to get free energy profiles. See more details in ref. [32] and in the online tutorial:
https://www.ks.uiuc.edu/Training/Tutorials/science/umbrella/REUS-1D.pdf

S1.2. Functional Modeling Methods

Drug – hERG interaction function scale model: The wild-type drug-free hERG Markov model was previously described in [1]. To simulate drug interactions with hERG, we used *simulated affinities* (i.e., drug dissociation constants), K_D, and drug diffusion rates, D, both computed from the umbrella sampling molecular dynamics (US-MD) simulations used to constrain the drug "on" (k_{o_d} and k_{od}) and "off" (r_{o_d} and r_{od}) model transition rates for open state. There are two modes of drug bound channel states – neutral (cyan) and cationic (red) for sotalol (see **Figure S2**).

The cationic and neutral drug fractions, f_1 and f_0, are calculated using the following equations:

$$f_1 = \frac{1}{(1+10^{(pH-pKa)})}; \quad f_0 = 1 - f_1 \qquad [1]$$

Where pH = 7.4 and pK_a = 8.3

Based on available literature data [33, 34], K_{DI} was assumed to be 63-fold less than K_{Do} in the model 2 (optimized using top-down approach, see main text) and 4.3-fold less than K_{Do} in the model 1. Then, using the relation, $k_{off} = k_{on} * K_{Do}$, we optimized k_{i_d} *and* k_{id} for open-inactivated state of neutral and cationic drugs.

Computed sotalol concentrations: We used the population C_{max} (maximum plasma concentration) of sotalol: 400 ng/ml to 1500 ng/ml [35], and converted it to micromolar (μM) concentrations: ($\frac{400\ ng/ml}{272.3624\ g/mol} \cong 1.4686\ \mu M$ to $\frac{1500\ ng/ml}{272.3624\ g/mol} \cong 5.5073\ \mu M$) in the models, where 272.3624 g/mol is sotalol molar mass.

Simulated beta adrenergic stimulations in the model: The O'Hara-Rudy human ventricular myocyte model [36], which includes effects of protein kinase A (PKA) on I_{caL}, I_{Ks}, I_{Kb}, I_{Na}, J_{rel}, J_{up}, troponin, and I_{Nak}, [37] was used to simulate QT interval. At the basal level, PKA effect was set to 0, and for control cases with beta adrenergic stimulation, PKA effect was set to 1 which is maximum effect. We assumed the range of effect is from 0 to 1 with linearly changes. Simulated effects of ISO (1 μM) on the endocardial action potentials are shown in **Figure S3**.

The addition of beta-blocking effect with sotalol was using the following equation:

$$\text{Beta blockade } = \frac{1}{1 + \frac{[Sotalol]}{K_i}}$$

where [Sotalol] is plasma drug concentration, and K_i is its beta-2 adrenergic receptor inhibitory constant, which is 38000 ng/ml for d-sotalol and 650 ng/ml for l-sotalol [38].

S1.3. Experimental Methods

Chemistry methods: Melting points were determined using a Büchi® B-540 melting point apparatus and are uncorrected. For HRMS analysis, samples were analyzed by flow-injection analysis into a Thermo Fisher Scientific LTQ Orbitrap XL (San Jose, CA) operated in profile mode. Source parameters were 5 kV spray voltage, capillary temperature of 275 ˚C and sheath gas setting of 20. Spectral data were acquired at a resolution setting of 100,000 FWHM with the lockmass feature which typically results in a mass accuracy < 2 ppm. ^{1}H-NMR and proton decoupled ^{13}C-NMR (^{13}C-NMR^{1}H) spectra were recorded on a Bruker 800 MHz Avance III Spectrometer equipped with a cryoprobe (University of California, Davis) with the mentioned solvents. Chemical shifts are reported in parts per million (ppm) on the δ scale and were referenced to the appropriate solvent peaks (CD_3OD referenced at δ_H = 3.31 ppm and δ_C = 49.1 ppm). NMR signal multiplicities are designated as follows: s (singlet), d

(doublet), septet (septet). Specific rotation, [α] and enantiomeric excess (ee) were determined using Rudolph Research Analytical Autopol IV, serial # 82182 polarimeter.

S- and *R*-sotalol crystals selected for crystal structure determination were mounted and optically centered in a nitrogen low temperature stream –183°C (90K), on the Bruker diffractometer with an APEX2 CCD detector or a Bruker D8 Venture diffractometer equipped with a Photon100 CMOS detector (Bruker, Madison, WI). Data were collected with the use of Mo Kα radiation in all cases (λ= 0.71073 Å). The structures were solved by direct methods (SHELXT) and refined by full-matrix least-squares on F^2 (SHELXL-2018/3). All non-hydrogen atoms were refined with anisotropic displacement parameters. For a description of the method, see [39].

Atomic coordinates of *S*-sotalol crystal are in the *Data Supplement* file and were also deposited to the Cambridge Structural Database with Deposition Number 2087412.

Separation of racemic sotalol into S- and R-sotalol: Sotalol hydrochloride was purchased from eNovation Chemicals LLC (Bridgewater, NJ, USA) and its identity and purity were confirmed by ^{1}H- and ^{13}C-NMR. In order to prepare free sotalol base, 5.0 g sotalol hydrochloride salt were dissolved in 23 mL methanol, and 2.5 mL KOH solution (7.0 M in MeOH) was added. Potassium chloride (KCl) immediately precipitated out as a white solid. The resulting suspension was vortexed thoroughly and then centrifuged. The clear supernatant was collected, and the solvent was evaporated under reduced pressure to obtain a glassy thick liquid which was then dissolved in ethyl acetate, filtered to remove minute quantities of potassium chloride and evaporated to obtain free base sotalol as a white amorphous solid. Yield: 4.4 g (99%). mp = 139.5-140.6°C. ^{1}H NMR (800 MHz, CD_3OD) δ 7.37 (d, J = 8.4 Hz, 2H), 7.25 (d, J = 8.4 Hz, 2H), 4.78 (dd, J_1 = 9.5 Hz, J_2 = 3.6 Hz, 1H), 3.02 (septet, J = 6.4 Hz, 1H), 2.93 (s, 3H), 2.88 (dd, J_1 = 12.2 Hz, J_2 = 3.6 Hz, 1H), 2.81 (dd, J_1 = 12.2 Hz, J_2 = 9.6 Hz, 1H), 1.17 (d, J = 6.4 Hz, 3H), 1.15 (d, J = 6.4 Hz, 3H). ^{13}C NMR (200 MHz, CD_3OD) δ 140.3, 139.4, 128.2, 121.8, 72.2, 54.8, 50.4, 39.2, 21.7, 21.6. HRMS (ESI) *m/z*: $(M + H)^+$ calcd. for $C_{12}H_{20}N_2O_3S$ 273.1267, found 273.1265.

Quantitative Separation of Sotalol Enantiomers Using Chiral HPLC: HPLC resolution of the two sotalol enantiomers from free base sotalol was performed with an Agilent 1100

HPLC (Agilent, Santa Clara, CA) equipped with a Chiralpak IA 4.6 X 250 mm column (Daicel Corp.), heated at 25°C. An isocratic solvent system consisting of 20% mobile phase A (ethanol with 0.1% diethyl amine) and 80% mobile phase B (hexane with 0.1% diethyl amine) was used for 15 min for each run. Sotalol was detected by its absorption at 220 nm using an Agilent 1100 diode array detector (DAD). Under these conditions (*S*) sotalol enantiomer has retention time t_R = 7.99 min. while (*R*) sotalol enantiomer has t_R = 11.88 min.

At a concentration of 10 mM, the two enantiomers, *S* and *R*, have a very good separation with 3.8 min difference between their retention times (t_R). This led us to try and separate the two enantiomers at increasingly higher concentrations. Thus 4 different sotalol solutions (10 mM, 100 mM, 160 mM and 220 mM) were used for this purpose. Even at 220 mM (60.6 mg/mL) sotalol shows non-overlapping, well-separated peaks of the two enantiomers (see *Data Supplement*). This enabled us to collect both enantiomers, in their pure form, while eluting from the small capacity analytical column by visually examining the real-time chromatogram. Using the method described above 25 µL of 220 mM sotalol (equivalent to 1.5 mg free base sotalol/injection) could easily be separated. The *S* enantiomer was collected (in glass test tubes) from 7.0 min to 9.2 min, while the *R* isomer was collected from 10.0 min to 13.3 min. Multiple runs using this method furnished about 25 mg of each enantiomer with almost 100% enantiomeric excess.

(*S*)-*N*-(4-(1-hydroxy-2-(isopropylamino)ethyl)phenyl)methanesulfonamide (S- / d- or (+)-sotalol) $[\alpha]^{25}_{D}$ = +17.4 (c = 0.32 in CH_3OH); ^{1}H NMR (800 MHz, CD_3OD) δ 7.34 (d, *J* = 8.4 Hz, 2H), 7.23 (d, *J* = 8.4 Hz, 2H), 4.72 (dd, J_1 = 9.2 Hz, J_2 = 3.8 Hz, 1H), 2.93 (s, 3H), 2.88 (septet, *J* = 6.4 Hz, 1H), 2.78 (dd, J_1 = 12.0 Hz, J_2 = 3.8 Hz, 1H), 2.72 (dd, J_1 = 12.0 Hz, J_2 = 9.2 Hz, 1H), 1.11 (d, *J* = 6.4 Hz, 3H), 1.08 (d, *J* = 6.4 Hz, 3H). ^{13}C NMR (200 MHz, CD_3OD) δ 140.8, 139.4, 128.2, 121.8, 72.9, 55.6, 49.9, 39.2, 22.5, 22.4. HRMS (ESI) *m/z*: $(M + H)^+$ calcd. for $C_{12}H_{20}N_2O_3S$ 273.1267, found 273.1265; ee (100 %) was determined by chiral HPLC (Chiralpak IA 4.6 X 250 mm column) using ethanol-hexane 20:80, 1 mL/min. (*S*)- enantiomer t_R = 7.99 min.

(*R*)-*N*-(4-(1-hydroxy-2-(isopropylamino)ethyl)phenyl)methanesulfonamide (R- / l- or (-)- sotalol) $[\alpha]^{25}_{D}$ = −35.3 (c = 0.31 in CH_3OH); ^{1}H NMR (800 MHz, CD_3OD) δ 7.36 (d, *J* =

8.4 Hz, 2H), 7.24 (d, J = 8.4 Hz, 2H), 4.76 (dd, J_1 = 9.4 Hz, J_2 = 3.6 Hz, 1H), 2.98 (septet, J = 6.4 Hz, 1H), 2.93 (s, 3H), 2.85 (dd, J_1 = 12.2 Hz, J_2 = 3.6 Hz, 1H), 2.78 (dd, J_1 = 12.1 Hz, J_2 = 9.4 Hz, 1H), 1.15 (d, J = 6.4 Hz, 3H), 1.13 (d, J = 6.4 Hz, 3H). ^{13}C NMR (200 MHz, CD_3OD) δ 140.5, 139.3, 128.2, 121.8, 72.4, 55.0, 50.2, 39.2, 21.95, 21.92. HRMS (ESI) *m/z*: $(M + H)^+$ calcd for $C_{12}H_{20}N_2O_3S$ 273.1267, found 273.1265; ee (99.6 %) was determined by chiral HPLC (Chiralpak IA 4.6 X 250 mm column) using ethanol-hexane 20:80, 1 mL/min. (*R*)- enantiomer t_R = 11.88 min.

Please see details in the *Data Supplement* and linked spectra files therein.

Electrophysiological recordings: A human embryonic kidney (HEK) 293 cell line stably expressing hERG was kindly provided by Dr. Craig T. January and maintained in minimum essential medium supplemented with 10% fetal bovine serum and 400 µg/ml G418 (Axenia Biologix, Dixon, CA) as previously described [40]. HEK cells were adhered to the poly-L-lysine-coated (MW 30,000-70,000, Sigma-Aldrich; 0.1 mg/mL for 2 hr at 37 ºC) coverslips in 12-well plates and transferred to a small recording chamber mounted on the stage of an inverted microscope (Axiovert S100, Carl Zeiss, Oberkochen, Germany), and were continuously superfused with HEPES-buffered Tyrode solution containing (in mM) 137 NaCl, 4 KCl, 1.8 $CaCl_2$, 1 $MgCl_2$, 10 glucose, and 10 HEPES (pH 7.4 with NaOH). Membrane currents were recorded in the whole-cell configuration established using pipette suction [41]. Leak compensation was not used. The borosilicate micropipette had a resistance of 2–4 MΩ when filled with the internal pipette solution contained (in mM) 120 KCl, 5.374 $CaCl_2$, 1.75 $MgCl_2$, 10 EGTA, 10 HEPES (pH 7.2 with KOH). Liquid junction potential with this internal solution was less than -4 mV, and the offset was not corrected. Series resistance was typically under 5 MΩ. Series resistance compensation was used when needed to constrain voltage error to <10 mV. Whole-cell recordings were performed using an Axopatch 200B patch-clamp amplifier (Molecular Devices, Sunnyvale, CA), ITC-18 interface and PatchMaster software (HEKA Elektronik, Lambrecht, Germany). The data were stored on a computer hard disk and analyzed using PatchMaster and Igor Pro 7 (WaveMetrics, Portland, OR). Experiments were performed at room temperature (22-25°C).

S2. Supplementary Tables

Table S1: **Transition rates in the I_{Kr} model**

Transition rates (ms^{-1})	
Drug free Kr channel	
C3→C2	$ae = \frac{T}{T_{base}} e^{(24.335+\frac{T_{base}}{T}(0.0112\times V-25.914))}$
C2→C3	$be = \frac{T}{T_{base}} e^{(13.688+\frac{T_{base}}{T}(-0.0603\times V-15.707))}$
C2→C1	$ain = \frac{T}{T_{base}} e^{(22.746+\frac{T_{base}}{T}(-25.914))}$
C1→C2	$bin = \frac{T}{T_{base}} e^{(13.193+\frac{T_{base}}{T}(-15.707))}$
C1→O	$aa = \frac{T}{T_{base}} e^{(22.098+\frac{T_{base}}{T}(0.0365\times V-25.914))}$
O→C1	$bb = \frac{T}{T_{base}} e^{(7.313+\frac{T_{base}}{T}(-0.0399\times V-15.707))}$
O→I	$\beta i = \frac{T}{T_{base}} e^{(30.016+\frac{T_{base}}{T}(0.0223\times V-30.88)} \times \left(\frac{5.4}{[K]^o}\right)^{0.4}$
I→O	$\alpha i = \frac{T}{T_{base}} e^{(30.061+\frac{T_{base}}{T}(-0.0312\times V-33.243))}$

Table S2: **Transition rates for d-sotalol – I_{Kr} (hERG) models**

model 1	**Open hERG (*x*=o)**	**Inactivated hERG (*x*=i)**
Transition rates	***Neutral drug (***K_{Do} = 173 μM)	
On (k_{x_d}**)**	7.4E+02 ($\mu M^{-1}s^{-1}$) * [drug]	8.3E+05 ($\mu M^{-1}s^{-1}$) * [drug]
Off (r_{x_d}**)**	1.3E+05 (s^{-1})	2.3E+06(s^{-1})
	Cationic drug (K_{Do} = 23,277 μM)	
On (k_{xd}**)**	3.6E+02 ($\mu M^{-1}s^{-1}$) * [drug]	8.8E+05 ($\mu M^{-1}s^{-1}$) * [drug]
Off (r_{xd}**)**	8.3E+06 (s^{-1})	3.3E+08(s^{-1})
model 2	**Open hERG (*x*=o)**	**Inactivated hERG (*x*=i)**
Transition rates	***Neutral drug***	
On (k_{x_d}**)**	7.4E+02 ($\mu M^{-1}s^{-1}$) * [drug]	137 ($\mu M^{-1}s^{-1}$) * [drug]
Off (r_{x_d}**)**	1.3E+05 (s^{-1})	5.5E+03 (s^{-1})
	Cationic drug	
On (k_{xd}**)**	3.6E+02 ($\mu M^{-1}s^{-1}$) * [drug]	4.96E+04 ($\mu M^{-1}s^{-1}$) * [drug]
Off (r_{xd}**)**	8.3E+06 (s^{-1})	2.7E+08 (s^{-1})

Table S3: **Transition rates for l-sotalol – I_{Kr} (hERG) models**

model 1	**Open hERG (*x*=o)**	**Inactivated hERG (*x*=i)**
Transition rates	***Neutral drug (*** K_{Do} = 595 μM)	
On (k_{x_d})	7.9E+02 ($\mu M^{-1}s^{-1}$) * [drug]	9.73E+05 ($\mu M^{-1}s^{-1}$) * [drug]
Off (r_{x_d})	4.7E+05 (s^{-1})	9.2E+06(s^{-1})
	Cationic drug (K_{Do} = 2,912 μM)	
On (k_{xd})	4.4E+02 ($\mu M^{-1}s^{-1}$) * [drug]	7.2E+05 ($\mu M^{-1}s^{-1}$) * [drug]
Off (r_{xd})	1.3E+06 (s^{-1})	3.3E+07(s^{-1})
model 2	**Open hERG (*x*=o)**	**Inactivated hERG (*x*=i)**
Transition rates	***Neutral drug***	
On (k_{x_d})	7.9E+02 ($\mu M^{-1}s^{-1}$) * [drug]	27 ($\mu M^{-1}s^{-1}$) * [drug]
Off (r_{x_d})	4.7E+05 (s^{-1})	3.7E+03 (s^{-1})
	Cationic drug	
On (k_{xd})	4.4E+02 ($\mu M^{-1}s^{-1}$) * [drug]	6.2E+04 ($\mu M^{-1}s^{-1}$) * [drug]
Off (r_{xd})	1.3E+06 (s^{-1})	4.2E+07 (s^{-1})

S3. Supplementary Figures

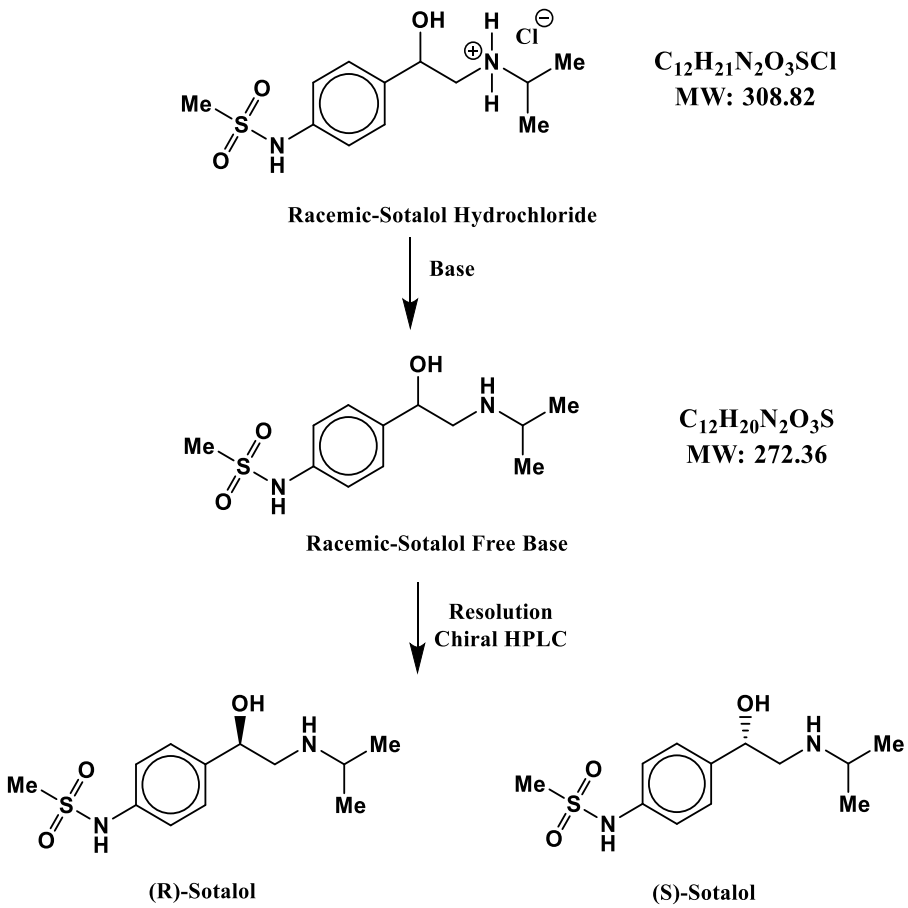

Figure S1. Schematics of an enantiomeric separation of l- / (R)- and d- / (S)-sotalol.

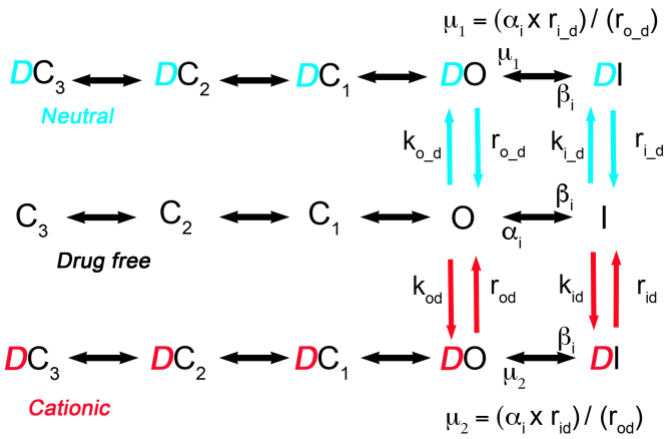

Figure S2. The Markov model represents a map of the hERG channel functional states. Drug free (black), cationic sotalol bound (red), and neutral sotalol bound (cyan) states are shown.

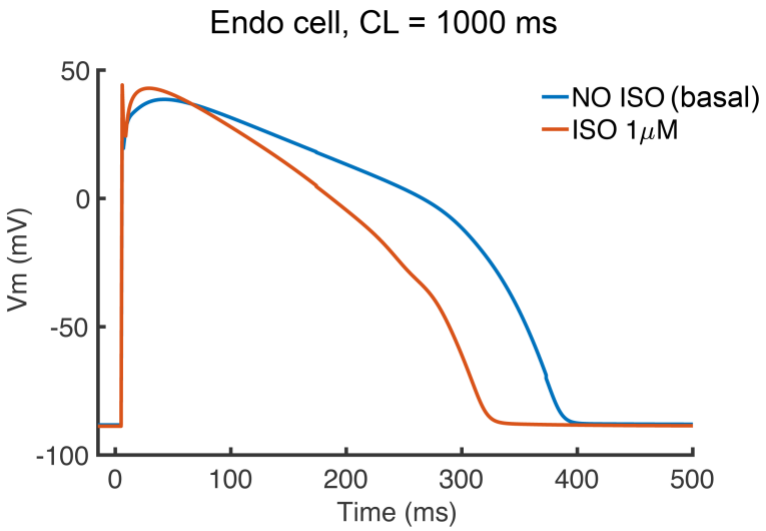

Figure S3. Simulated effects of ISO (1 μM) on the endocardial action potential at cycle length (CL) of 1000 ms compared to basal level of action potential.

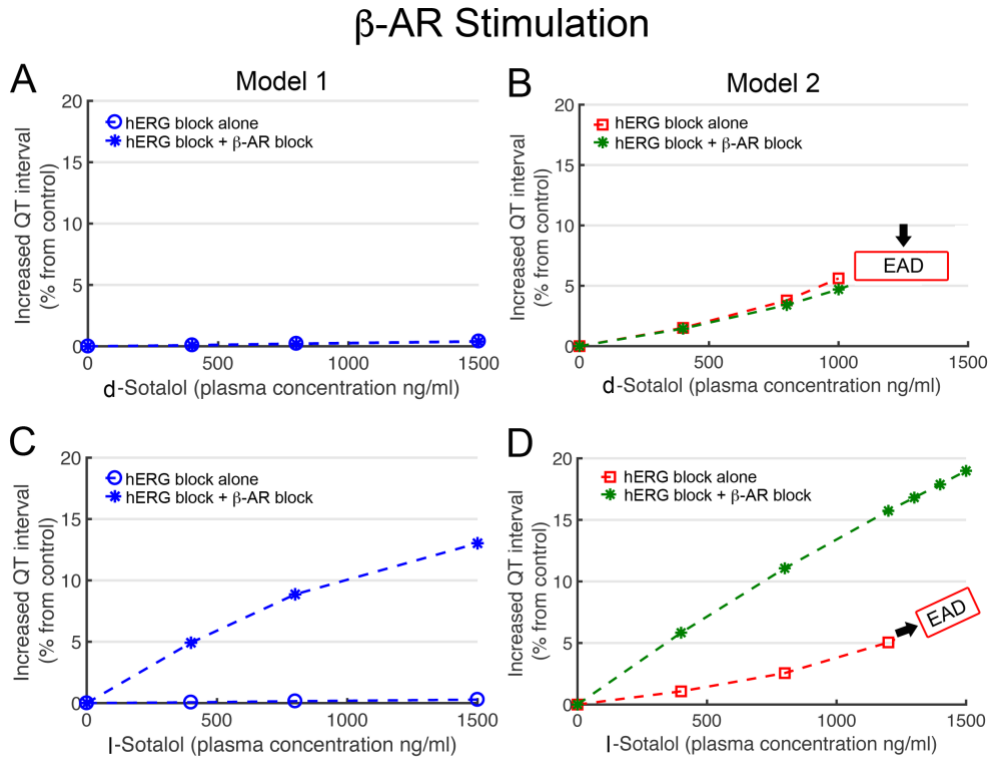

Figure S4. Prediction of the effect of varying sotalol concentrations during isoproterenol (ISO) application with or without simulated βAR blockade by sotalol. A pseudo ECG (QT interval) was computed from a one-dimensional strand of O'Hara-Rudy human cardiac ventricular myocytes at 1 Hz pacing for a range of d- and l-sotalol concentrations for model 1 fit to HEK cell line data from this work (blue, panels **A** and **C**) and model 2 fit to guinea pig ventricular myocyte data from ref. [33] (red and green, panels **B** and **D**). See main text for more details. **(A)** During 1 μM ISO application, model 1 shows no QT interval effect with increasing d-sotalol concentration **(B)** During 1 μM ISO application, model 2 predicts a concentration dependent increase by up to 5% in QT interval by d-sotalol on hERG block alone (red squares) and with simulated sotalol-induced βAR blockade (green asterisks). Early afterdepolarizations (EADs) were observed at 1200 ng/ml d-sotalol during 1μM ISO application after 200 seconds with hERG block alone. **(C)** During 1 μM ISO application, model 1 shows no QT intervals changes with increasing l-sotalol plasma concentrations accounting for hERG block alone. On the contrary, up to 13% QT interval prolongation occurs with increasing l-sotalol plasma concentration when hERG block and βAR block are both simulated. **(D)** During 1 μM ISO application, simulations with model 2 predicted plasma concentration dependent QT interval increase by l-sotalol with hERG block alone (red squares), by up to 5%, and also when l-sotalol-induced βAR blockade was simulated (green asterisks), by up to 19%. EADs were observed at 1200 ng/ml with hERG block alone during 1μM ISO application after 700 seconds.

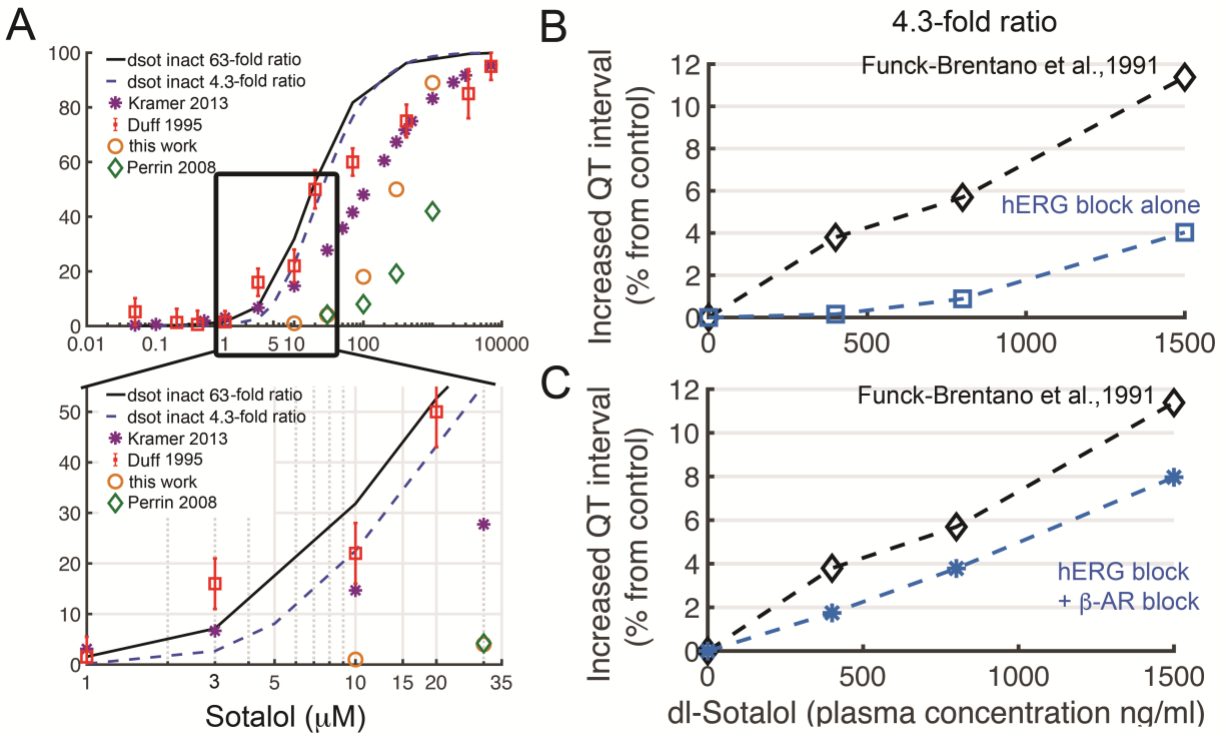

Figure S5. Concentration dependent block of hERG and QT prolongation by sotalol using alternative models. **(A)** Experimentally measured dose dependent inhibition of hERG by sotalol (colored symbols) and model optimization for d-sotalol using data from ref. [33] for fitting as well as two different estimates for open/inactivated hERG block ratio: 63-fold ratio of sotalol IC_{50} values for low/high dofetilide affinity sites from ref. [33] (solid black line) or 4.3 fold ratio of sotalol IC_{50} values for S620T mutant to WT hERG in Chinese hamster ovary (CHO) cells from ref. [34] (dashed dark-blue line). Experimental data are from: Kramer 2013 – ref. [42]; Duff 1995 – ref. [33]; Perrin 2008 – ref. [34]. The inset focuses on data for clinically relevant drug concentrations. Panels **B** and **C** show dl-sotalol concentration dependent QT prolongation data for a model with a 4.3-fold open/inactivated hERG block ratio. **(B)** Concentration dependent increase in QT intervals by d,l-sotalol with hERG channel block alone (blue squares) compared to clinical data (black diamonds) from ref. [35]. (C) During sympathetic stimulation via concurrent ISO 1μM application, simulations showed a concentration dependent increase in QT interval by d,l-sotalol dependent hERG block and βAR blockade (blue asterisks) compared to clinical data from ref. [35] (black diamonds).

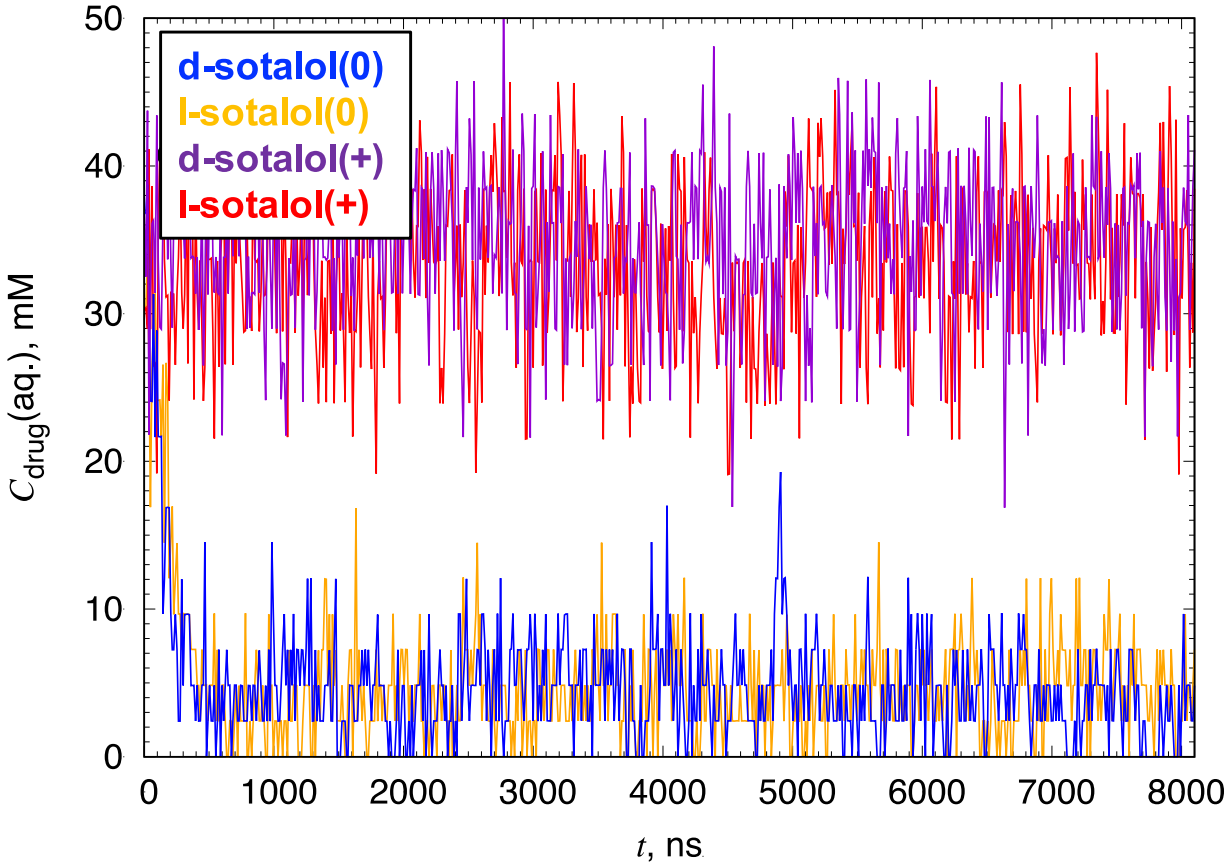

Figure S6. Sotalol aqueous concentration time series from hERG channel – drug flooding 8.1 μs long MD simulations on Anton 2 supercomputer. These data indicate that while most cationic d- and l-sotalol(+) molecules remain in aqueous solution, neutral d- and l-sotalol(0) bulk aqueous concentration decreases dramatically due to drug binding to the hERG channel and/or lipid membrane.

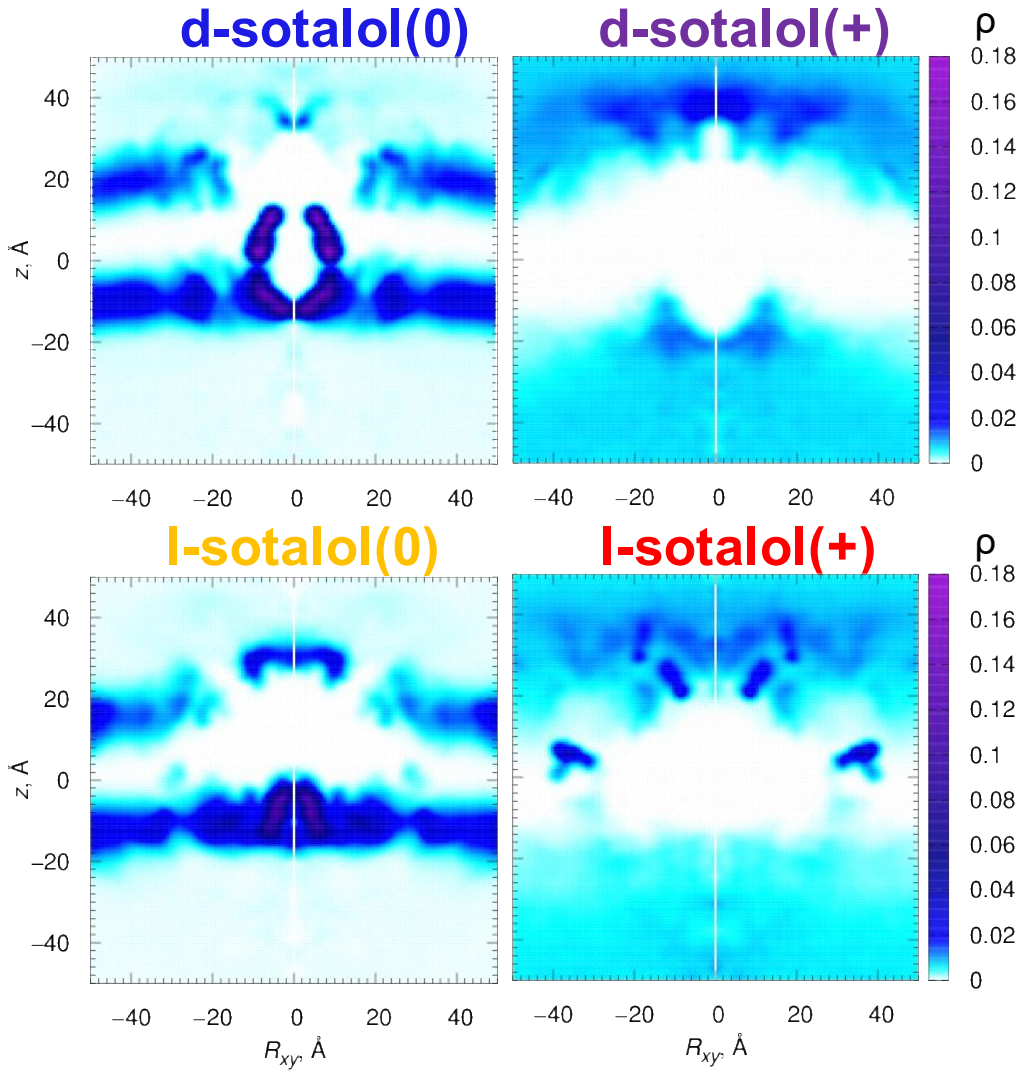

Figure S7. Two-dimensional weighted atomic density distributions of sotalol molecules from hERG channel – sotalol flooding 8 microsecond long MD production runs on Anton 2 supercomputer (with the initial 90 ns equilibration runs excluded from this analysis) . Three-dimensional time-averaged volumetric map obtained using VMD *volmap* script was converted to an averaged and symmetrized two-dimensional cylindrical distributions using the z axis and the lateral distance R_{xy} from the z axis as coordinates. Color bars on the right indicate averaged atomic density, ρ, range from 0 to 0.18. The hERG channel appearing as a white spot at the center is embedded in the POPC membrane centered around z = 0. Dark-blue and violet spots indicate high sotalol density concentrations due to binding to the hERG channel and/or lipid membrane. Light-blue shades at the top and bottom indicate time-averaged sotalol density in bulk aqueous solution.

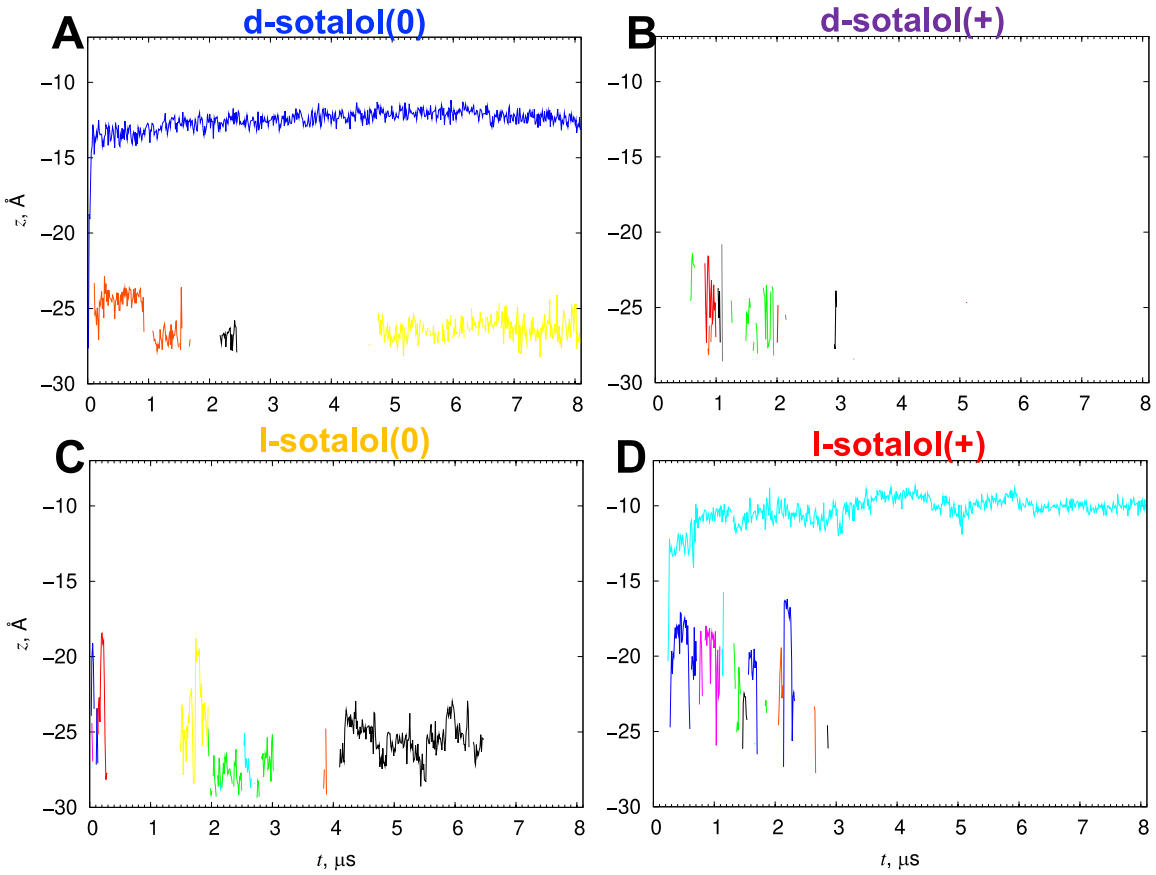

Figure S8. Time series of sotalol binding events to hERG channel as measured by drug presence within the pore during 8.1 μs long drug flooding simulation**.** For each trace, the *z*-position of a sotalol molecule is reported over time only when its center of mass is within a cylinder of radius 8 Å and height of 40 Å that encompasses the hERG channel pore.

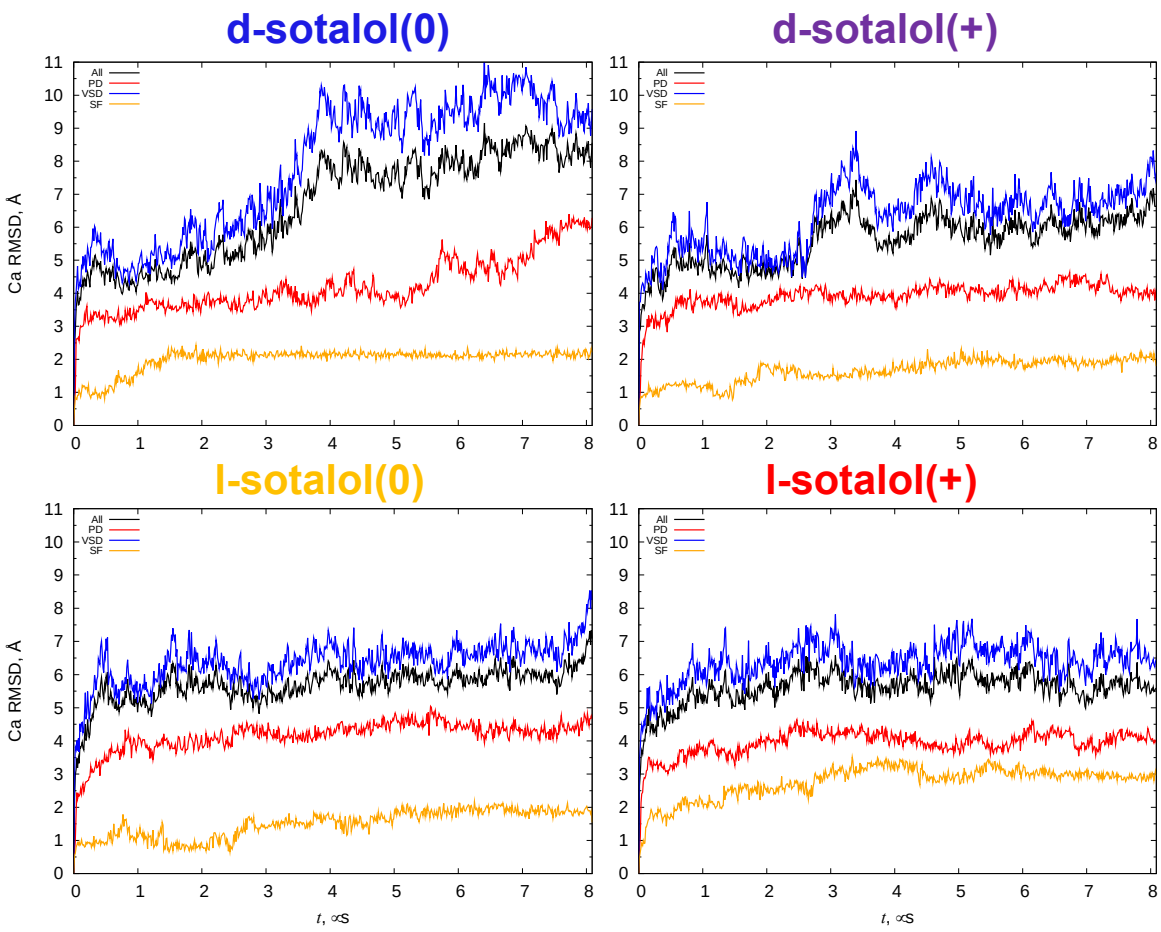

Figure S9. Time series of hERG channel root-mean-square deviation (RMSD) profiles for the entire protein model (All), pore domain (PD), voltage-sensing domain (VSD) and selectivity filter (SF) C_α protein backbone atoms from 8.1 microsecond long hERG – sotalol flooding MD simulations.

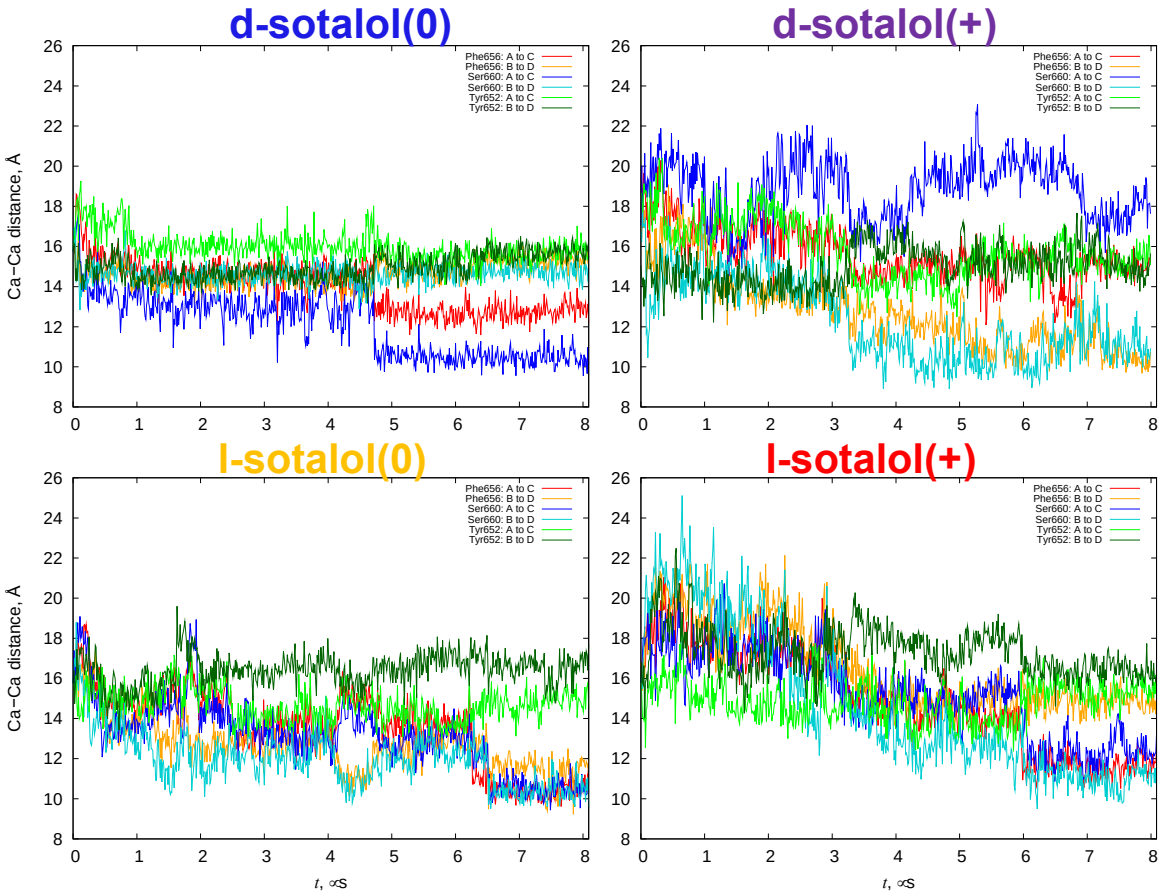

Figure S10. Time series of distances between C_α protein backbone atoms of hERG S6 segment residues Tyr652 (Y652), Phe656 (F656), and Ser660 (S660) of two opposite chains (A and C, B and D) from 8.1 μs long drug flooding hERG – sotalol MD simulations. A substantial decrease in those distances over the course of the simulations indicates hERG channel pore closure.

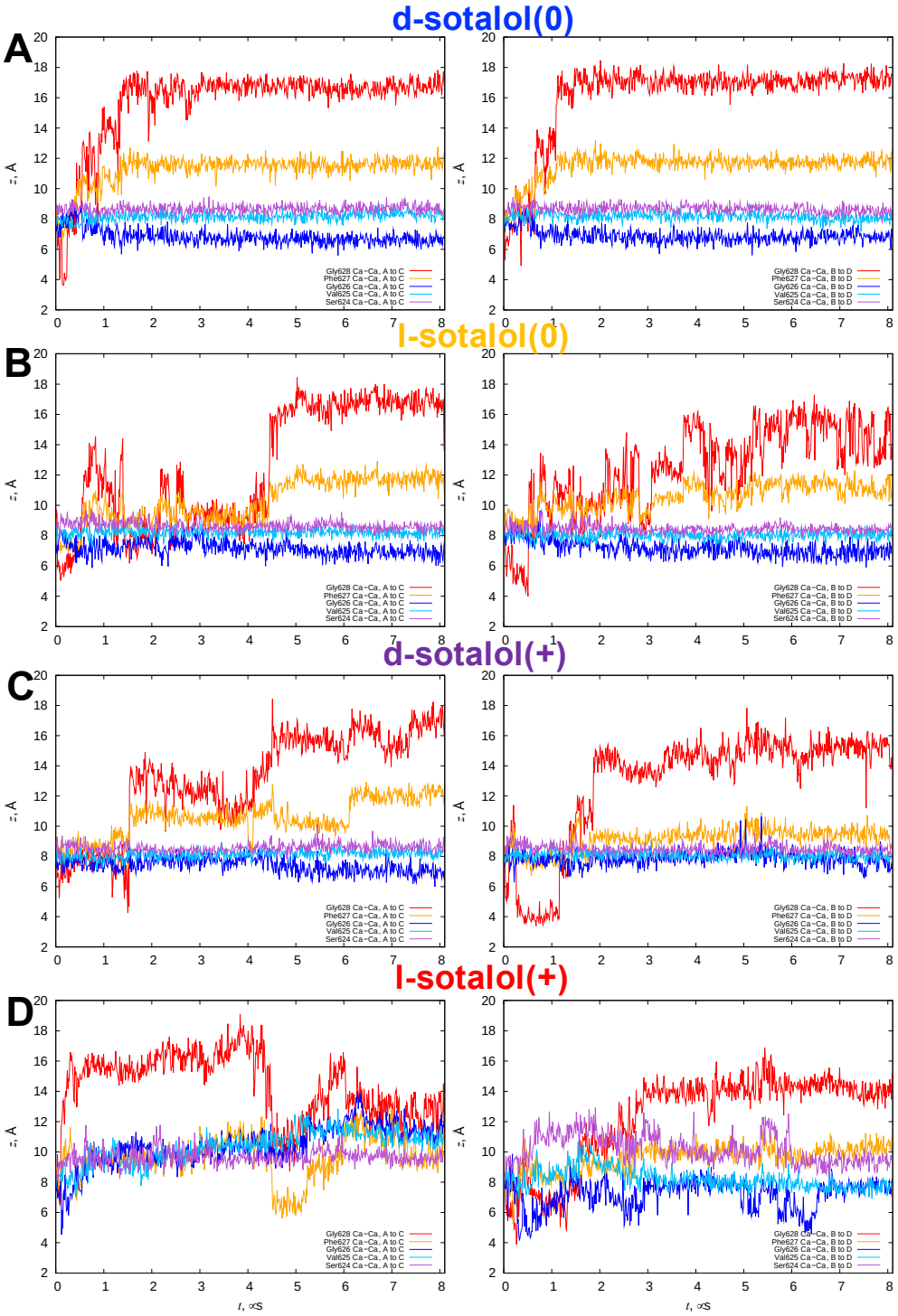

Figure S11. Time series of distances between C_α protein backbone atoms of hERG selectivity filter (SF) residues Ser624 (S624), Val625 (V625), Gly626 (G626), Phe627 (F627), and Gly628 (G628) of 2 opposite chains, A and C (left panels), B and D (right panels) from 8.1 μs long drug flooding hERG – sotalol MD simulations, which indicate significant SF distortions.

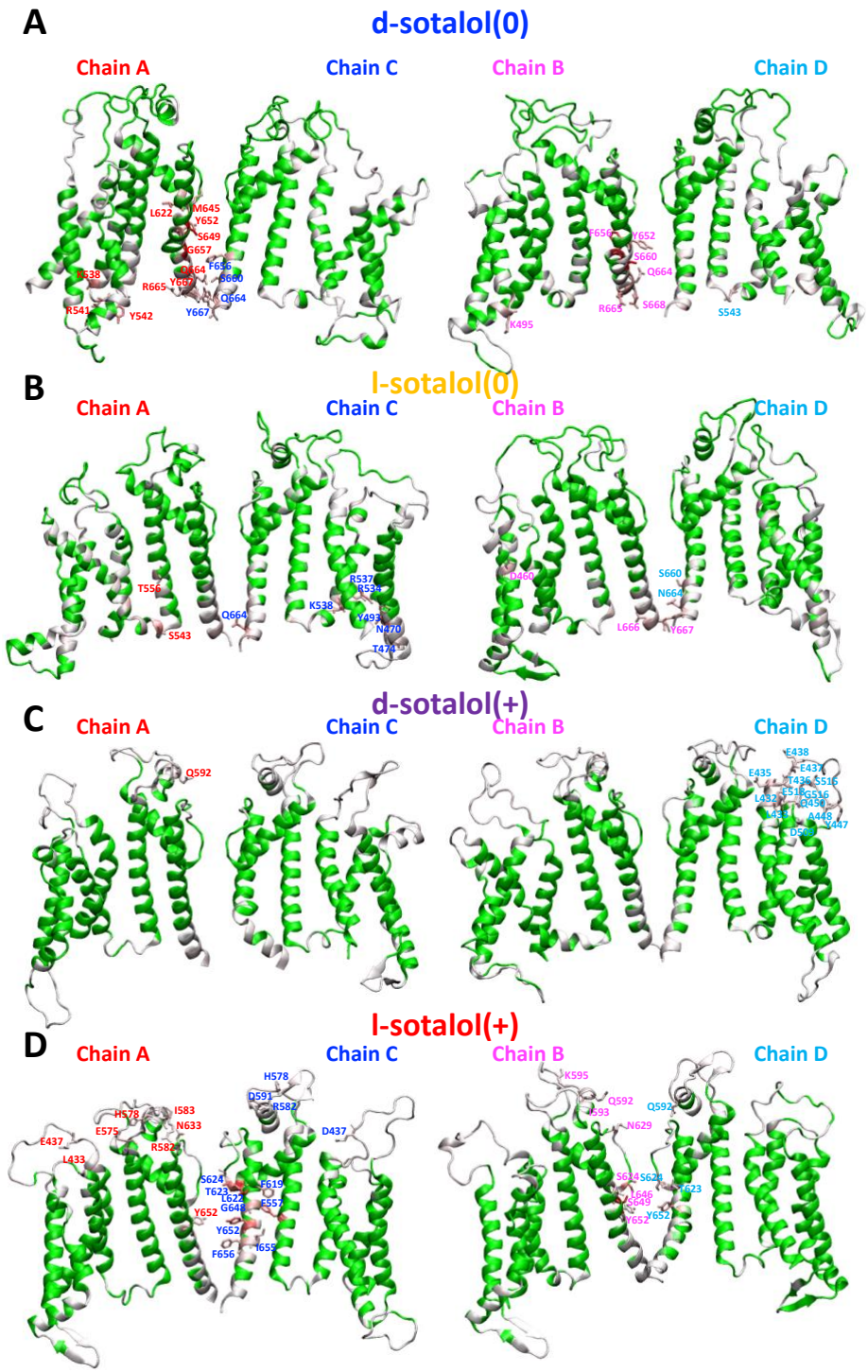

Figure S12. Neutral (0) and cationic (+) d- and l-sotalol interactions with hERG channel residues from 8 μs long drug flooding MD production runs. Final channel structures with non-interacting residues are in green, interacting – white to red for interaction frequencies from 1 to 100%. hERG residues with interaction frequency ≥20% for sotalol(0) and ≥10% for sotalol(+) are shown as sticks and labeled. Interaction is established if a distance between non-hydrogen atoms of sotalol and hERG channel is within 3.5 Å. See also ***Fig. S13***.

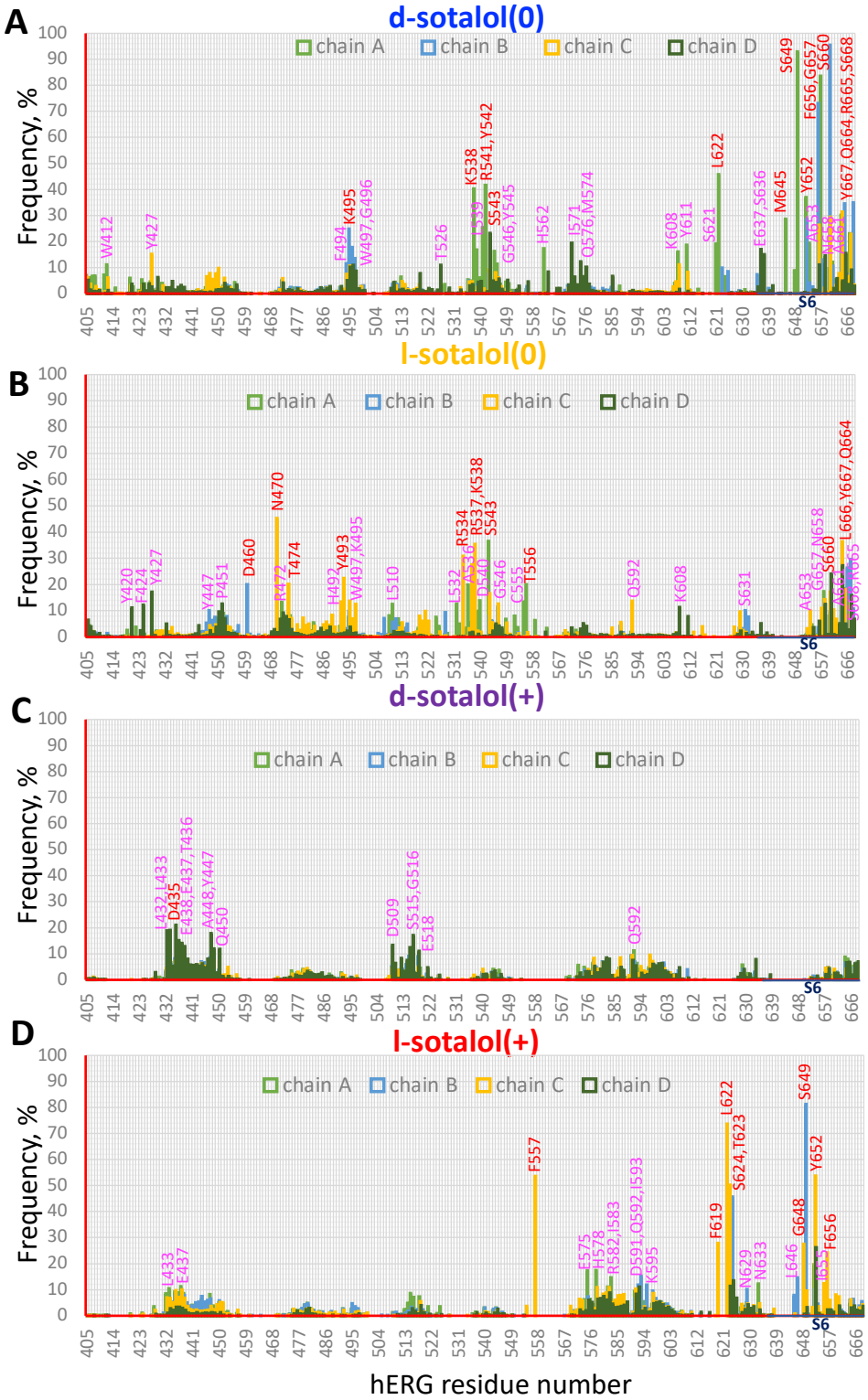

Figure S13. Histograms for frequencies of interactions between neutral (0) and cationic (+) d- and l-sotalol with hERG channel residues from 8 μs long drug flooding MD production runs. hERG residues with interaction frequency ≥20% are labeled in red and those with frequencies between 10 and 20% in magenta. Interaction is established if a distance between non-hydrogen atoms of sotalol and hERG channel is within 3.5 Å. See also ***Fig. S12***.

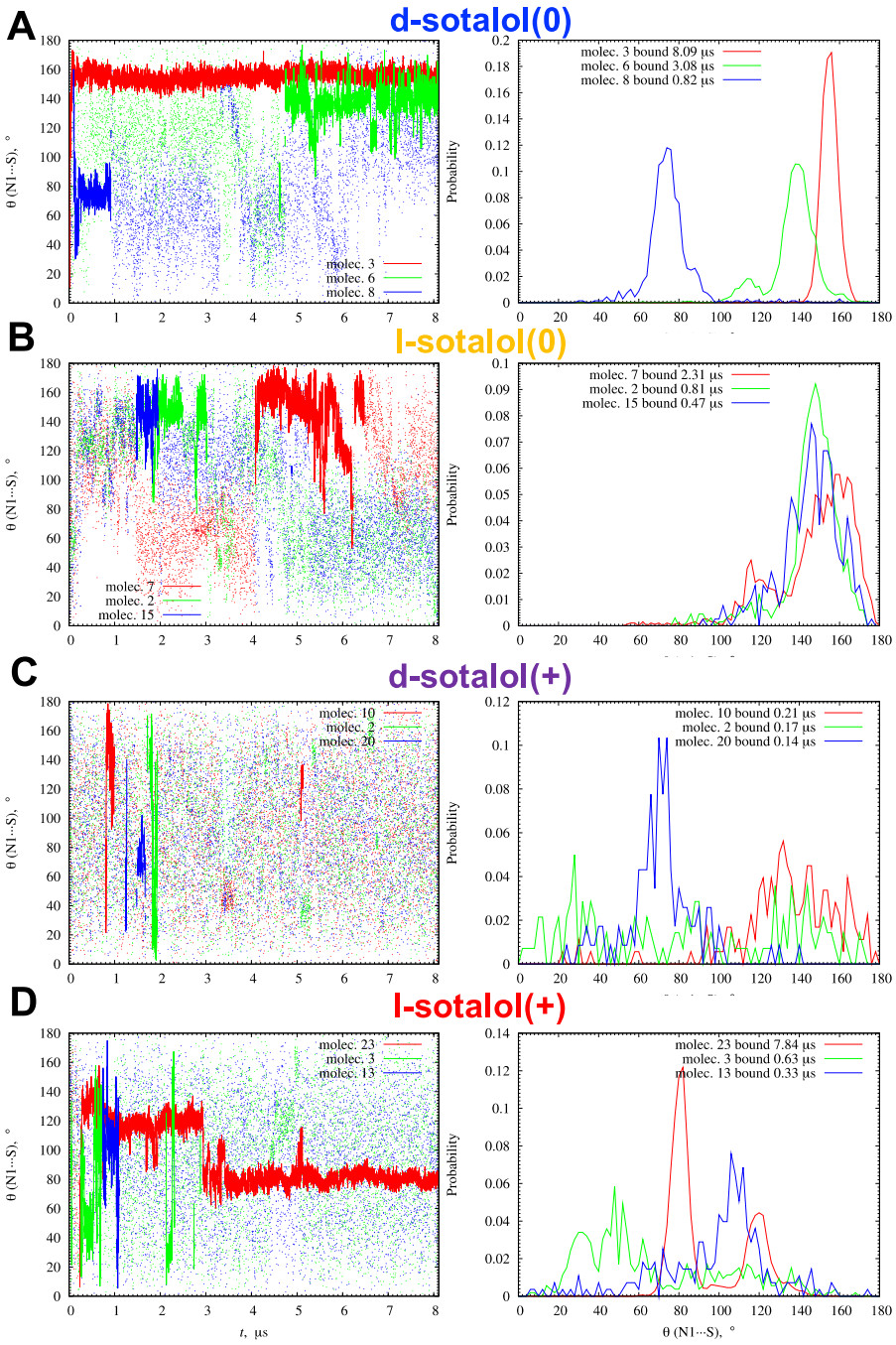

Figure S14. Drug tumbling analysis from 8.1 μs long hERG – sotalol flooding MD simulations. *Left panels:* time series of a polar angle θ between sotalol N1···S vector and the *z* axis for 3 molecules bound for the longest simulation times. Bound states – thick lines, unbound – dots. *Right panels:* histogram distributions of those polar angles for bound states only.

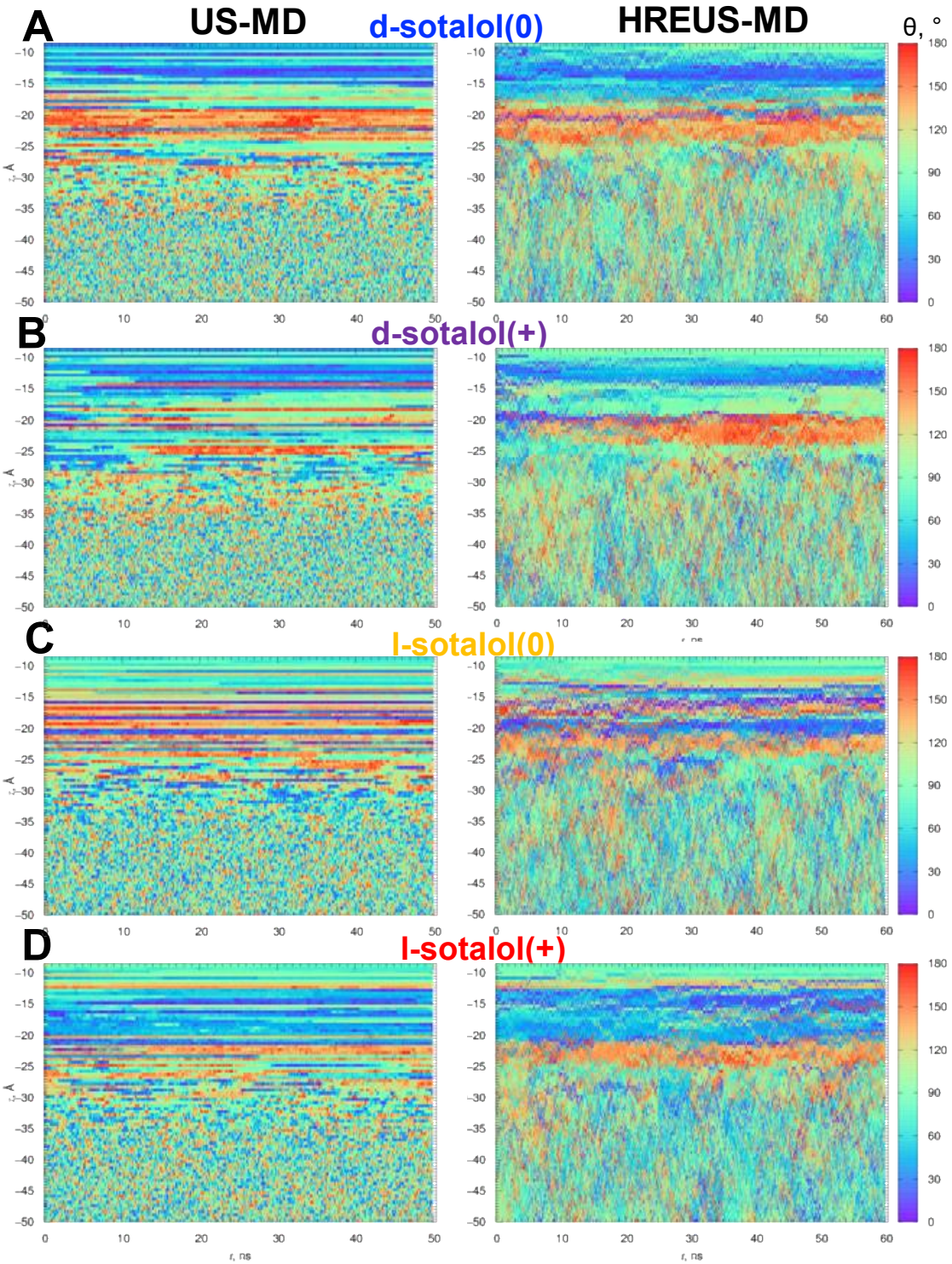

Figure S15. Time series of sotalol orientation during US-MD (left) and HREUS-MD (right) MD simulations of open-state hERG channel as judged by the polar angle θ of sotalol N1···S vector with the *z* axis. Color palette corresponds to θ range from 0° to 180° (see bars on the right). The *y* axis corresponds to US-MD or HREUS-MD reaction coordinate – drug's center of mass (COM) *z* position with respect to the COM of hERG selectivity filter C_α atoms.

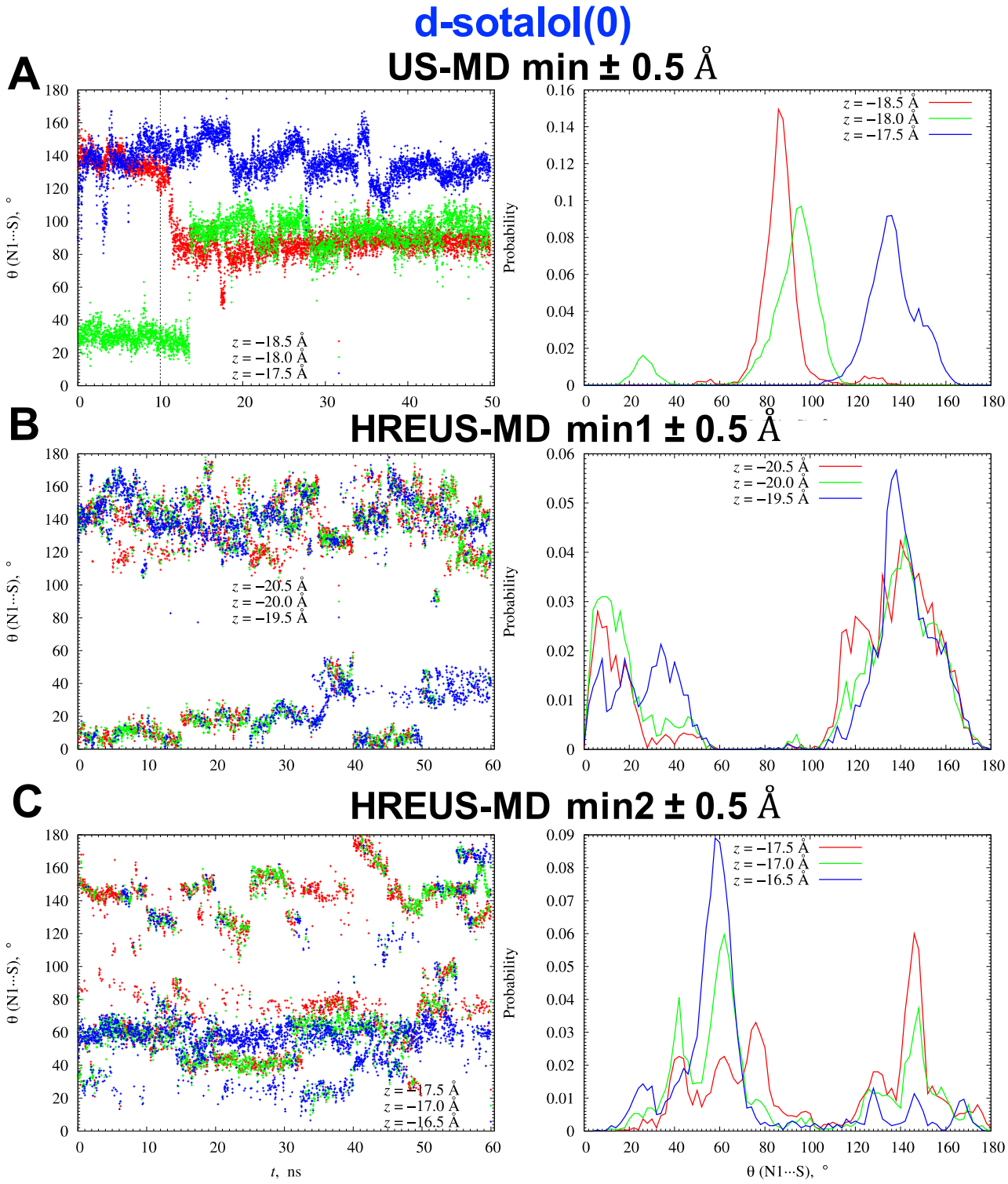

Figure S16. Time series of d-sotalol(0) orientation during US-MD (*panel A*) and HREUS-MD (*panels B&C*) MD simulations of an open state hERG binding as judged by the polar angle θ of sotalol N1···S vector with the *z* axis. *Left panels:* time series of θ around US-MD or HREUS-MD minima. *Right panels:* histogram distributions of θ for these US-MD or HREUS-MD windows (first 10 ns of US-MD runs are not included in the histogram analyses).

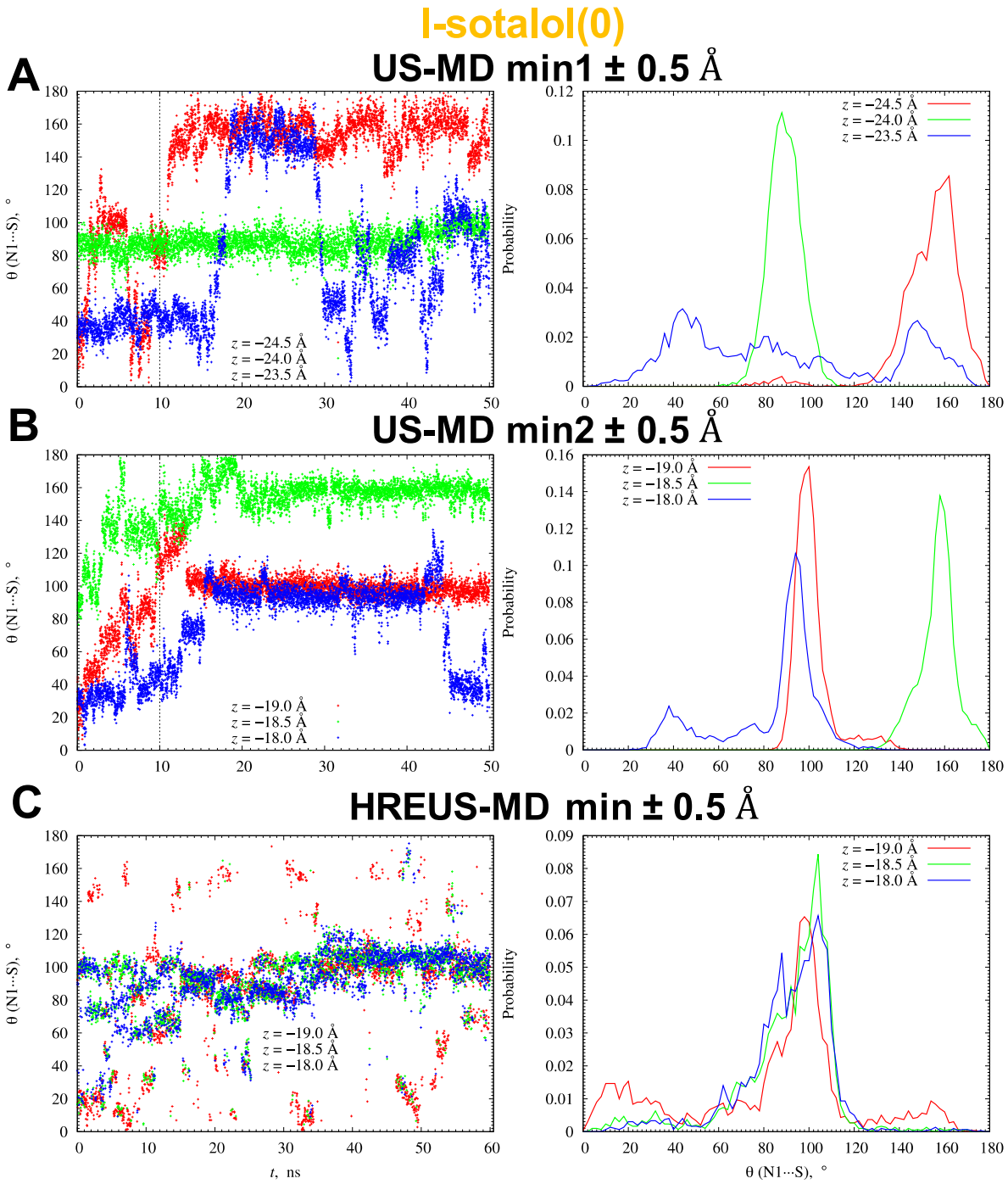

Figure S17. Time series of l-sotalol(0) orientation during US-MD (*panels A&B*) and HREUS-MD (*panel C*) MD simulations of an open state hERG binding as judged by the polar angle θ of sotalol N1···S vector with the *z* axis. *Left panels:* time series of θ around US-MD or HREUS-MD minima. *Right panels:* histogram distributions of θ for these US-MD or HREUS-MD windows (first 10 ns of US-MD runs are not included in the histogram analyses).

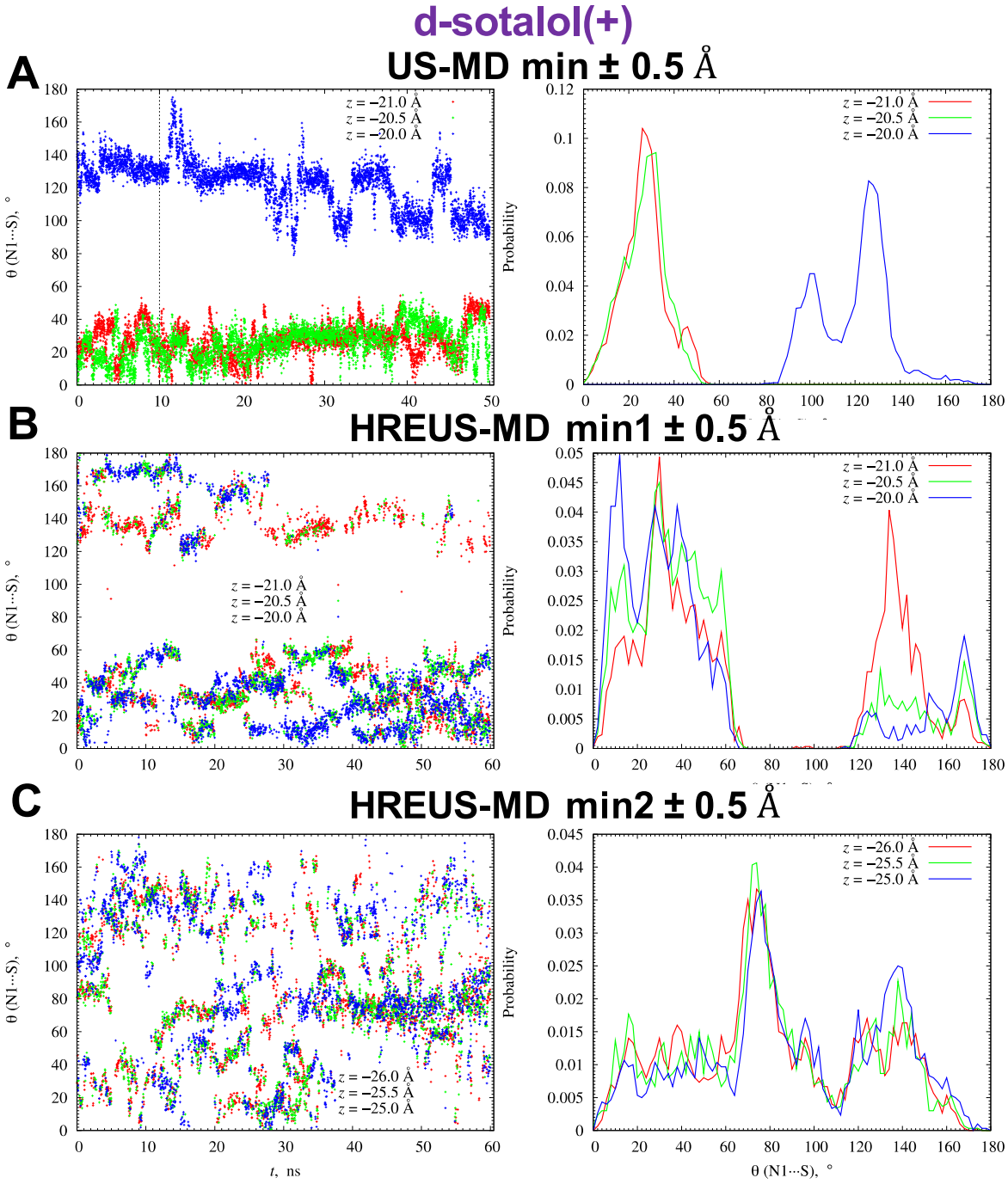

Figure S18. Time series of d-sotalol(+) orientation during US-MD (*panel A*) and HREUS-MD (*panels B&C*) MD simulations of an open state hERG binding as judged by the polar angle θ of sotalol N1···S vector with the *z* axis. *Left panels:* time series of θ around US-MD or HREUS-MD minima. *Right panels:* histogram distributions of θ for these US-MD or HREUS-MD windows (first 10 ns of US-MD runs are not included in the histogram analyses).

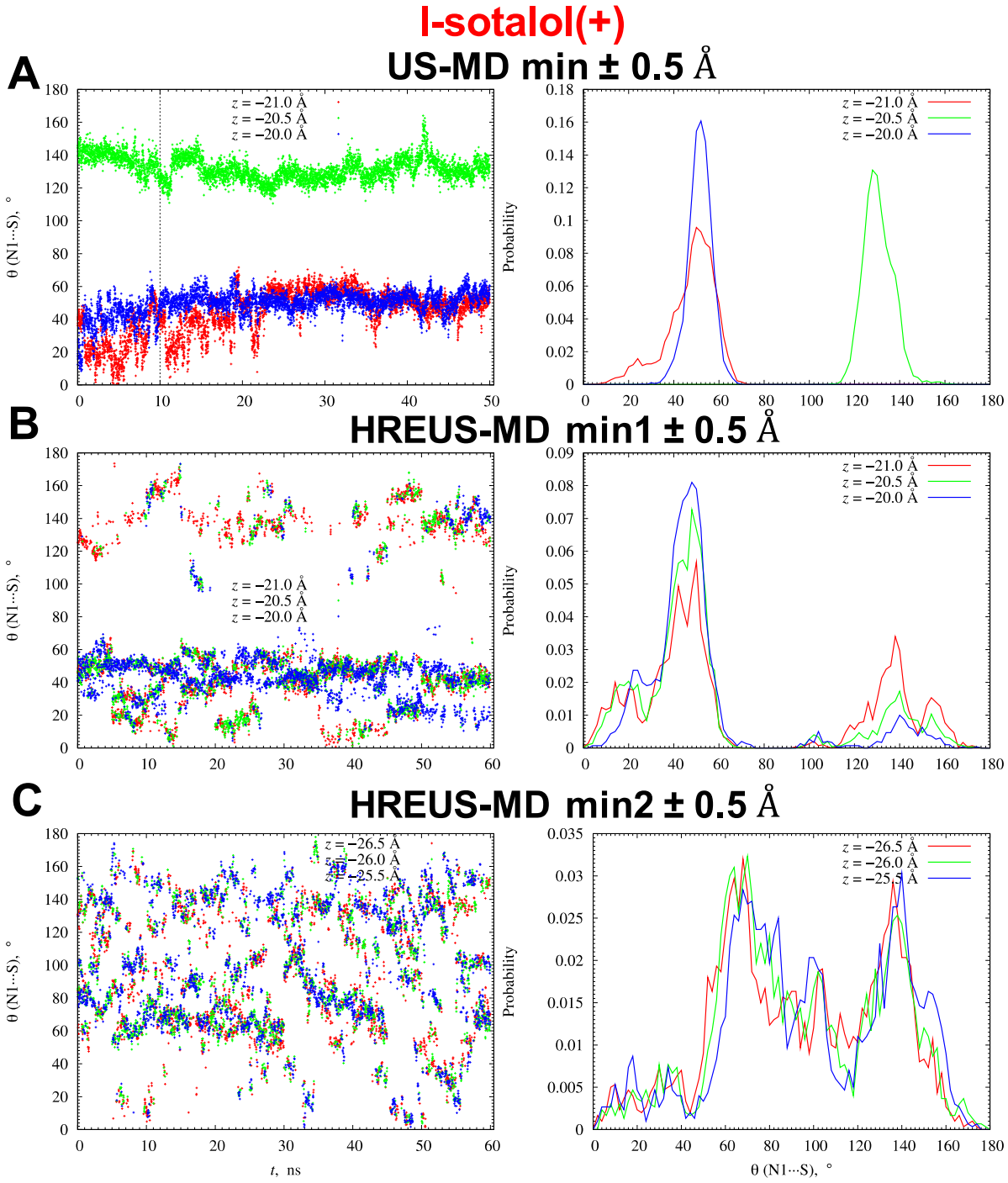

Figure S19. Time series of l-sotalol(+) orientation during US-MD (*panel A*) and HREUS-MD (*panels B&C*) MD simulations of an open state hERG binding as judged by the polar angle θ of sotalol N1···S vector with the *z* axis. *Left panels:* time series of θ around US-MD or HREUS-MD minima. *Right panels:* histogram distributions of θ for these US-MD or HREUS-MD windows (first 10 ns of US-MD runs are not included in the histogram analyses).

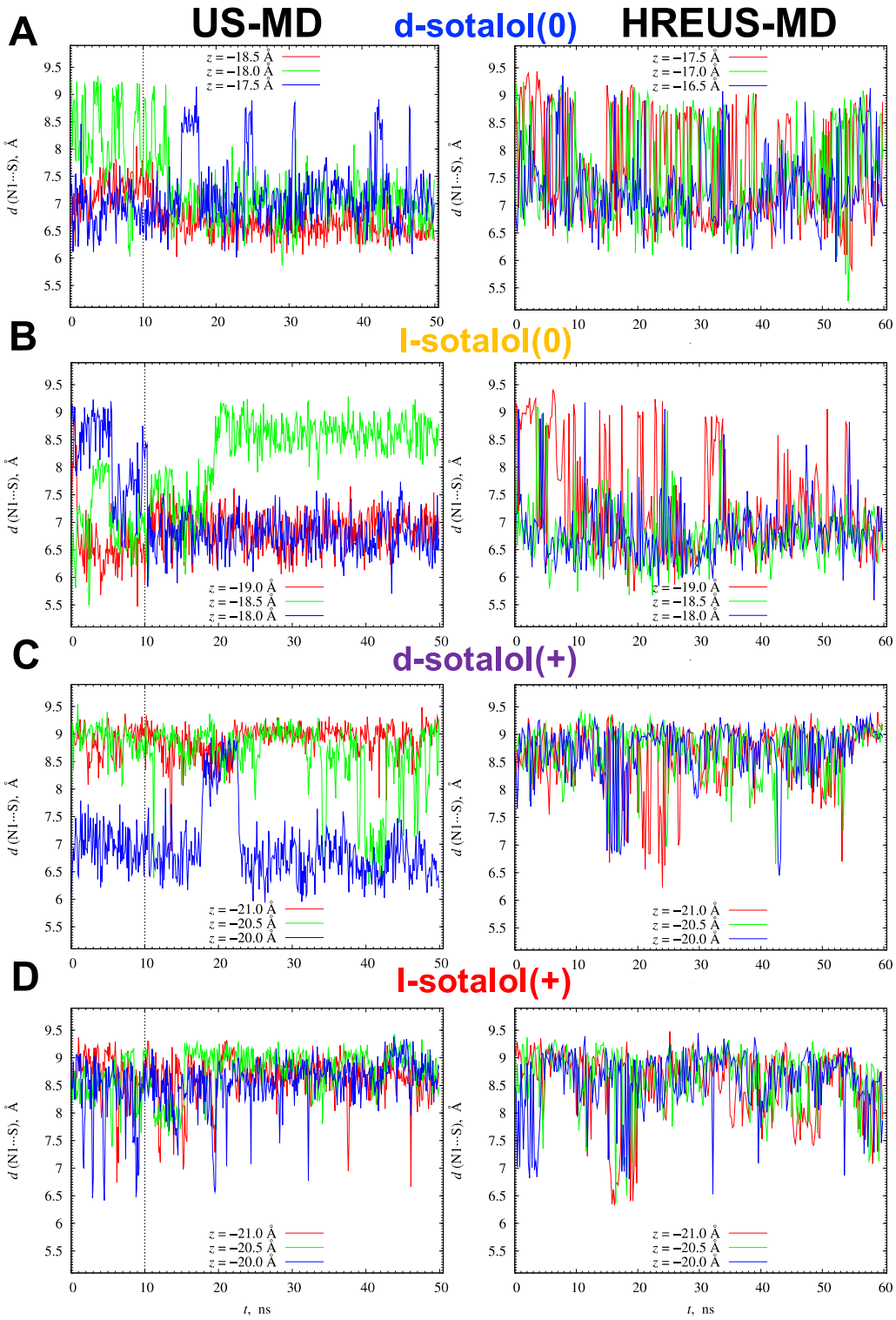

Figure S20. Time series of sotalol molecule conformational changes estimated from the length of N1···S vector, *d*(N1···S), during US-MD (*left panels*) and HREUS-MD (*right panels*) simulations of an open state hERG binding for selected frames around corresponding free energy minima. Data indicate rapid conformational changes during HREUS-MD runs (*right panels*) and much more restricted but still existing changes during US-MD runs (*left panels*).

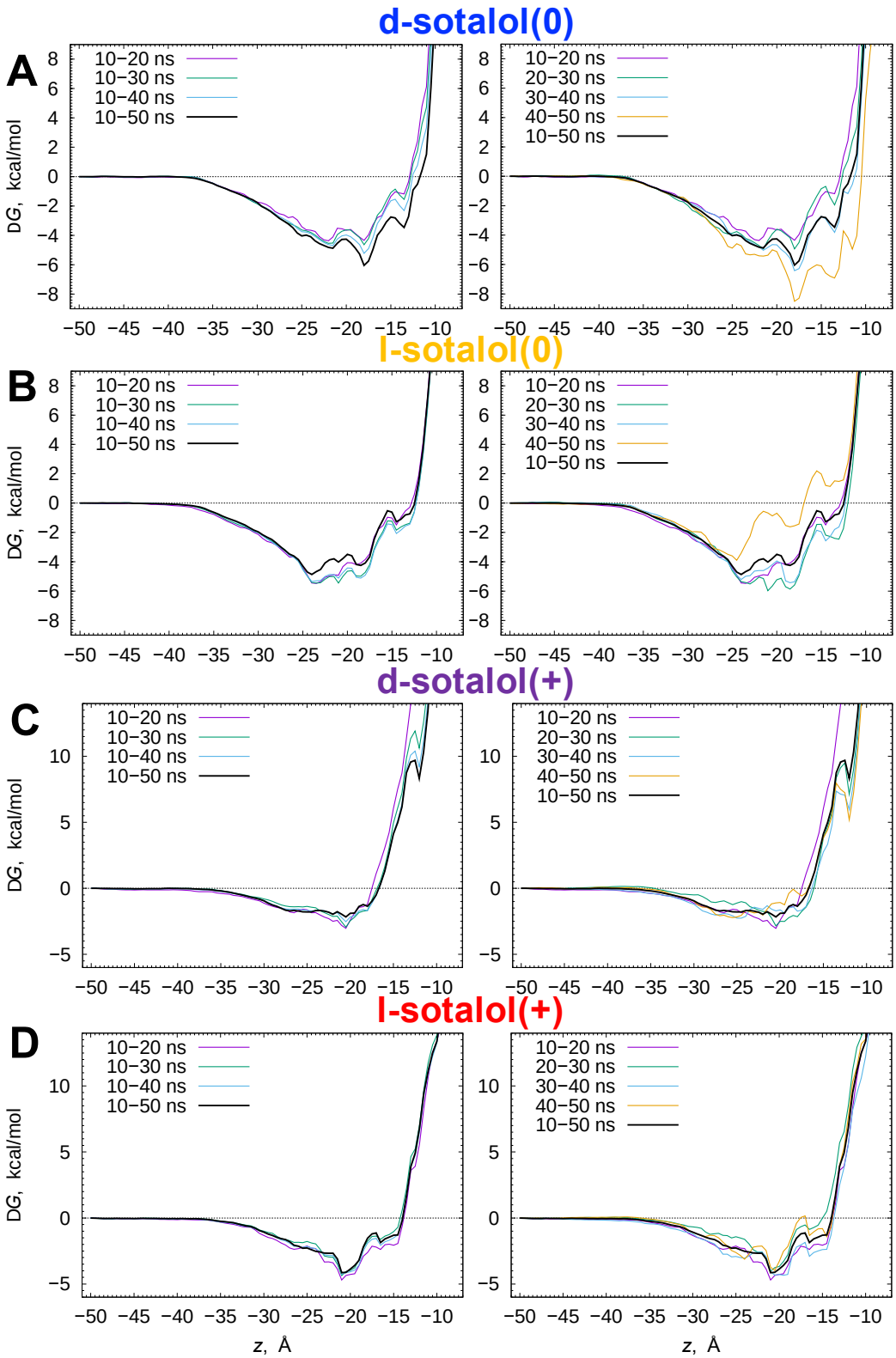

Figure S21. Convergence of free energy profiles from umbrella sampling MD (US-MD) simulations of sotalol binding to open state hERG channel. *Left panels:* free energy profiles from 10 up to 50 ns in 10-ns increments. *Right panels:* free energy profiles for 10 ns blocks.

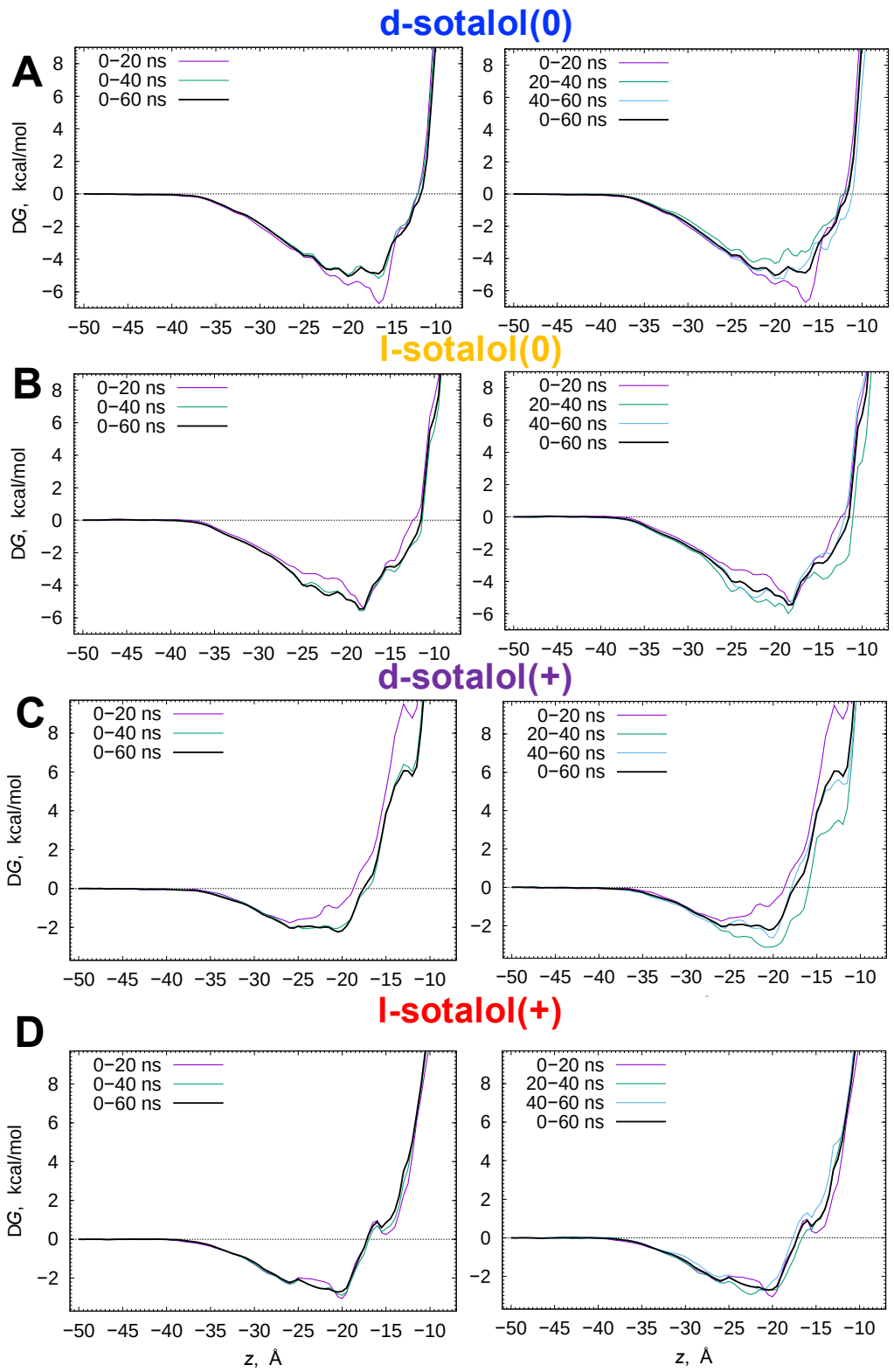

Figure S22. Convergence of free energy profiles from Hamiltonian replica exchange umbrella sampling MD (HREUS-MD) simulations of sotalol binding to open state hERG channel. *Left panels:* free energy profiles from 0 up to 60 ns in 20 ns increments. *Right panels:* free energy profiles for 20-ns blocks.

S4. Supplementary References

[1] P.C. Yang, K.R. DeMarco, P. Aghasafari, M.T. Jeng, J.R. Dawson, S. Bekker, S. Noskov, V. Yarov-Yarovoy, I. Vorobyov, C.E. Clancy, A Computational Pipeline to Predict Cardiotoxicity:From the Atom to the Rhythm, Circ Res 126 (2020) 947-964.
[2] W. Wang, R. MacKinnon, Cryo-EM Structure of the Open Human Ether-a-go-go-Related K+ Channel hERG, Cell 169(3) (2017) 422-430 e10.
[3] V. Yarov-Yarovoy, J. Schonbrun, D. Baker, Multipass membrane protein structure prediction using Rosetta, Proteins 62(4) (2006) 1010-25.
[4] P. Barth, J. Schonbrun, D. Baker, Toward high-resolution prediction and design of transmembrane helical protein structures, Proc Natl Acad Sci U S A 104(40) (2007) 15682-7.
[5] I. Andre, P. Bradley, C. Wang, D. Baker, Prediction of the structure of symmetrical protein assemblies, Proc Natl Acad Sci U S A 104(45) (2007) 17656-61.
[6] K.R. DeMarco, S. Bekker, C.E. Clancy, S.Y. Noskov, I. Vorobyov, Digging into Lipid Membrane Permeation for Cardiac Ion Channel Blocker d-Sotalol with All-Atom Simulations, Front Pharmacol 9 (2018) 26.
[7] K. Vanommeslaeghe, A.D. MacKerell, Automation of the CHARMM General Force Field (CGenFF) I: Bond Perception and Atom Typing, J Chem Inf Model 52(12) (2012) 3144-3154.
[8] K. Vanommeslaeghe, E.P. Raman, A.D. MacKerell, Automation of the CHARMM General Force Field (CGenFF) II: Assignment of Bonded Parameters and Partial Atomic Charges, J Chem Inf Model 52(12) (2012) 3155-3168.
[9] C.G. Mayne, J. Saam, K. Schulten, E. Tajkhorshid, J.C. Gumbart, Rapid Parameterization of Small Molecules Using the Force Field Toolkit, J Comput Chem 34(32) (2013) 2757-2770.
[10] W. Humphrey, A. Dalke, K. Schulten, VMD: visual molecular dynamics, J Mol Graph 14(1) (1996) 33-8, 27-8.
[11] M. Frisch, G. Trucks, H. Schlegel, G. Scuseria, M. Robb, J. Cheeseman, G. Scalmani, V. Barone, B. Mennucci, G. Petersson, Gaussian 09. Wallingford, CT: Gaussian, Inc, 2009.
[12] K. Vanommeslaeghe, E. Hatcher, C. Acharya, S. Kundu, S. Zhong, J. Shim, E. Darian, O. Guvench, P. Lopes, I. Vorobyov, A.D. MacKerell, CHARMM General Force Field: A Force Field for Drug-Like Molecules Compatible with the CHARMM All-Atom Additive Biological Force Fields, J Comput Chem 31(4) (2010) 671-690.
[13] S. Jo, T. Kim, V.G. Iyer, W. Im, CHARMM-GUI: a web-based graphical user interface for CHARMM, J Comput Chem 29(11) (2008) 1859-65.
[14] J.C. Phillips, R. Braun, W. Wang, J. Gumbart, E. Tajkhorshid, E. Villa, C. Chipot, R.D. Skeel, L. Kale, K. Schulten, Scalable molecular dynamics with NAMD, J Comput Chem 26(16) (2005) 1781-1802.
[15] D.E. Shaw, J.P. Grossman, J.A. Bank, B. Batson, J.A. Butts, J.C. Chao, M.M. Deneroff, R.O. Dror, A. Even, C.H. Fenton, A. Forte, J. Gagliardo, G. Gill, B. Greskamp, C.R. Ho, D.J. Ierardi, L. Iserovich, J.S. Kuskin, R.H. Larson, T. Layman, L.S. Lee, A.K. Lerer, C. Li, D. Killebrew, K.M. Mackenzie, S.Y.H. Mok, M.A. Moraes, R. Mueller, L.J. Nociolo, J.L. Peticolas, T. Quan, D. Ramot, J.K. Salmon, D.P. Scarpazza, U. Ben Schafer, N. Siddique, C.W. Snyder, J. Spengler, P.T.P. Tang, M. Theobald, H. Toma, B. Towles, B. Vitale, S.C. Wang, C. Young, Anton 2: Raising the bar for performance and programmability in a special-purpose molecular dynamics supercomputer, Int Conf High Perfor (2014) 41-53.
[16] J. Huang, A.D. MacKerell, Jr., CHARMM36 all-atom additive protein force field: validation based on comparison to NMR data, J Comput Chem 34(25) (2013) 2135-45.

[17] R.B. Best, X. Zhu, J. Shim, P.E. Lopes, J. Mittal, M. Feig, A.D. MacKerell Jr, Optimization of the additive CHARMM all-atom protein force field targeting improved sampling of the backbone ϕ, ψ and side-chain χ1 and χ2 dihedral angles, J Chem Theory Comput 8(9) (2012) 3257-3273.
[18] J.B. Klauda, R.M. Venable, J.A. Freites, J.W. O'Connor, D.J. Tobias, C. Mondragon-Ramirez, I. Vorobyov, A.D. MacKerell, Jr., R.W. Pastor, Update of the CHARMM all-atom additive force field for lipids: validation on six lipid types, J Phys Chem B 114(23) (2010) 7830-43.
[19] W.L. Jorgensen, J. Chandrasekhar, J.D. Madura, R.W. Impey, M.L. Klein, Comparison of Simple Potential Functions for Simulating Liquid Water, J Chem Phys 79(2) (1983) 926-935.
[20] S.E. Feller, Y. Zhang, R.W. Pastor, B.R. Brooks, Constant pressure molecular dynamics simulation: The Langevin piston method, J Chem Phys103(11) (1995) 4613-4621.
[21] S. Nosé, A unified formulation of the constant temperature molecular dynamics methods, J Chem Phys 81(1) (1984) 511-519.
[22] W.G. Hoover, Canonical dynamics: Equilibrium phase-space distributions, Phys Rev A 31(3) (1985) 1695-1697.
[23] J.-P. Ryckaert, G. Ciccotti, H.J.C. Berendsen, Numerical integration of the cartesian equations of motion of a system with constraints: molecular dynamics of n-alkanes, J Comput Phys 23(3) (1977) 327-341.
[24] T. Darden, D. York, L. Pedersen, Particle mesh Ewald: An N·log(N) method for Ewald sums in large systems, J Chem Phys 98(12) (1993) 10089-10092.
[25] J. Lee, X. Cheng, J.M. Swails, M.S. Yeom, P.K. Eastman, J.A. Lemkul, S. Wei, J. Buckner, J.C. Jeong, Y.F. Qi, S. Jo, V.S. Pande, D.A. Case, C.L. Brooks, A.D. MacKerell, J.B. Klauda, W. Im, CHARMM-GUI Input Generator for NAMD, GROMACS, AMBER, OpenMM, and CHARMM/OpenMM Simulations Using the CHARMM36 Additive Force Field, J Chem Theory Comput 12(1) (2016) 405-413.
[26] K.R. DeMarco, J.R. Dawson, P.-C. Yang, S. Bekker, V.A. Ngo, S.Y. Noskov, V. Yarov-Yarovoy, C.E. Clancy, I. Vorobyov, Atomistic modeling towards predictive cardiotoxicity, bioRxiv (2019) 635441.
[27] R.A. Lippert, C. Predescu, D.J. Ierardi, K.M. Mackenzie, M.P. Eastwood, R.O. Dror, D.E. Shaw, Accurate and efficient integration for molecular dynamics simulations at constant temperature and pressure, J Chem Phys 139(16) (2013) 10B621_1.
[28] G.J. Martyna, D.J. Tobias, M.L. Klein, Constant pressure molecular dynamics algorithms, J Chem Phys 101(5) (1994) 4177-4189.
[29] G.M. Torrie, J.P. Valleau, Nonphysical sampling distributions in Monte Carlo free-energy estimation: Umbrella sampling, J Comput Phys 23(2) (1977) 187-199.
[30] S. Kumar, J.M. Rosenberg, D. Bouzida, R.H. Swendsen, P.A. Kollman, THE weighted histogram analysis method for free-energy calculations on biomolecules. I. The method, J Comput Chem 13(8) (1992) 1011-1021.
[31] B. Isralewitz, M. Gao, K. Schulten, Steered molecular dynamics and mechanical functions of proteins, Curr Opin Struct Biol 11(2) (2001) 224-230.
[32] W. Jiang, Y. Luo, L. Maragliano, B. Roux, Calculation of free energy landscape in multi-dimensions with Hamiltonian-exchange umbrella sampling on petascale supercomputer, J Chem Theory Comput 8(11) (2012) 4672-4680.
[33] H.J. Duff, Z.P. Feng, R.S. Sheldon, High- and low-affinity sites for [3H]dofetilide binding to guinea pig myocytes, Circ Res 77(4) (1995) 718-25.
[34] M.J. Perrin, P.W. Kuchel, T.J. Campbell, J.I. Vandenberg, Drug binding to the inactivated state is necessary but not sufficient for high-affinity binding to human ether-a-go-go-related gene channels, Mol Pharmacol 74(5) (2008) 1443-52.

[35] C. Funck-Brentano, Y. Kibleur, F. Le Coz, J.M. Poirier, A. Mallet, P. Jaillon, Rate dependence of sotalol-induced prolongation of ventricular repolarization during exercise in humans, Circulation 83(2) (1991) 536-45.
[36] T. O'Hara, L. Virág, A. Varró, Y. Rudy, Simulation of the undiseased human cardiac ventricular action potential: model formulation and experimental validation, PLoS Comput Biol 7(5) (2011) e1002061.
[37] T. O'Hara, Y. Rudy, Arrhythmia formation in subclinical ("silent") long QT syndrome requires multiple insults: quantitative mechanistic study using the KCNQ1 mutation Q357R as example, Heart Rhythm 9(2) (2012) 275-82.
[38] C. Funck-Brentano, D.J. Silberstein, D.M. Roden, A.J. Wood, R.L. Woosley, A mechanism of D-(+)-sotalol effects on heart rate not related to beta-adrenoceptor antagonism, Br J Clin Pharmacol 30(2) (1990) 195-202.
[39] G.M. Sheldrick, A short history of SHELX, Acta Crystallogr, Sect A 64 (2008) 112-121.
[40] Z. Zhou, Q. Gong, B. Ye, Z. Fan, J.C. Makielski, G.A. Robertson, C.T. January, Properties of HERG channels stably expressed in HEK 293 cells studied at physiological temperature, Biophys J 74(1) (1998) 230-241.
[41] O.P. Hamill, A. Marty, E. Neher, B. Sakmann, F. Sigworth, Improved patch-clamp techniques for high-resolution current recording from cells and cell-free membrane patches, Pflügers Archiv 391(2) (1981) 85-100.
[42] J. Kramer, C.A. Obejero-Paz, G. Myatt, Y.A. Kuryshev, A. Bruening-Wright, J.S. Verducci, A.M. Brown, MICE models: superior to the HERG model in predicting Torsade de Pointes, Sci Rep 3(1) (2013) 1-7.